AGU100 ADVANCING EARTH AND SPACE SCIENCE

Water Resources Research

RESEARCH ARTICLE
10.1029/2018WR023586

Remote Sensing of River Bathymetry: Evaluating a Range of Sensors, Platforms, and Algorithms on the Upper Sacramento River, California, USA

Carl J. Legleiter[1,2] **and Lee R. Harrison**[3,4]

[1]Integrated Modeling and Prediction Division, U.S. Geological Survey, Golden, CO, USA, [2]Department of Geography, University of Wyoming, Laramie, WY, USA, [3]Southwest Fisheries Science Center, National Oceanic and Atmospheric Administration, Santa Cruz, CA, USA, [4]Earth Research Institute, University of California, Santa Barbara, CA, USA

Key Points:
- Accurate depths were retrieved from satellite images, hyperspectral data acquired from manned and unmanned aircraft, and a bathymetric LiDAR
- Generalized Optimal Band Ratio Analysis allows flexible calibration of spectral quantities to depth; exponential model avoids artifacts
- The maximum detectable depth is a key constraint on fluvial remote sensing, particularly for LiDAR due to a lack of bottom returns >2 m

Supporting Information:
- Supporting Information S1

Correspondence to:
C. J. Legleiter,
cjl@usgs.gov

Citation:
Legleiter, C. J., & Harrison, L. R. (2019). Remote sensing of river bathymetry: Evaluating a range of sensors, platforms, and algorithms on the upper Sacramento River, California, USA. *Water Resources Research*, *55*, 2142–2169. https://doi.org/10.1029/2018WR023586

Received 27 JUN 2018
Accepted 17 DEC 2018
Accepted article online 27 DEC 2018
Published online 19 MAR 2019

Abstract Remote sensing has become an increasingly viable tool for characterizing fluvial systems. In this study, we used field measurements with a 1.6-km reach of the upper Sacramento River, CA, to evaluate the potential of mapping water depths with a range of platforms, sensors, and depth retrieval methods. Field measurements of water column optical properties also were compared to similar data sets from other rivers to provide context for our results. We considered field spectra, a multispectral satellite image, hyperspectral data collected from conventional and unmanned aircraft, and a bathymetric LiDAR and applied a generalized version of Optimal Band Ratio Analysis and the *K* nearest neighbors regression machine learning algorithm. Linear, quadratic, exponential, power, and lowess Optimal Band Ratio Analysis models enabled flexible curve-fitting in calibrating spectrally based quantities to depth; an exponential formulation avoided artifacts associated with other model types. *K* nearest neighbors regression increased observed versus predicted (OP) R^2 values, particularly for the satellite image; we also found that preprocessing of satellite images was unnecessary and that a basic data product could be used for depth retrieval. Bathymetric LiDAR was highly accurate and precise in shallow water, but a lack of bottom returns from areas greater than 2 m deep resulted in large gaps in coverage. The maximum detectable depth imposes an important constraint on fluvial remote sensing and a hybrid approach combined with field surveys of deep areas might be a more realistic operational strategy for bathymetric mapping. Future work will focus on scaling up from short reaches to long river segments.

1. Introduction

Spatially distributed information on water depth is vital to studies in fluvial geomorphology and stream ecology and also plays a central role in many river management applications (e.g., Benjankar et al., 2018), particularly those that involve in-stream habitat assessment (e.g., McKean et al., 2008; McKean & Tonina, 2013). Given the difficulty and expense of measuring depths via conventional field methods, remote sensing of river bathymetry has become an increasingly appealing alternative. The development of new sensors, platforms, and algorithms, along with their greater availability and ease of use, has spurred significant progress in fluvial remote sensing. Entwistle et al. (2018) reviewed these advances and reiterated the claim that "the time for more widespread application of river remote sensing techniques is now" (Marcus & Fonstad, 2010, p. 1867). Moreover, Entwistle et al. (2018) exhorted the research community to use these methods to generate "new insights and ideas on fluvial form and function, … challenging paradigms and moving the science forward." This goal has become more realistic as the cost of acquiring remotely sensed data, particularly with unmanned aircraft systems (UASs), has decreased. Although a certain degree of optimism is justified, further testing and refinement of remote sensing methods is needed to optimize our ability to infer river information and to define realistic expectations. Such a pragmatic approach would facilitate informed, effective use of these rapidly evolving technologies. More specifically, direct, comparative evaluations conducted in a range of fluvial environments become more valuable as the number of instruments and means of deploying them continues to grow (Legleiter et al., 2016). In this study, we assess the potential to map water depths along a short reach of a large (>100 m wide) gravel-bed river with a number of different sensors, platforms, and depth retrieval algorithms. Although our focus herein is on estimating depth, bed elevation is the variable of interest for many applications (Carbonneau et al., 2011; Kammel et al., 2016). Whereas depth depends on

discharge, bed elevation is independent of flow stage and is the primary input variable required for hydrodynamic modeling (e.g., Bovee, 1978; Leclerc et al., 1995; Pasternack et al., 2004). Submerged topography can be derived from a depth map via a relatively simple workflow: Given an independent source of information on water surface elevation, such as conventional near-infrared (NIR) LiDAR, image-derived depth estimates can be subtracted from water surface elevations to obtain bed elevations (e.g., Legleiter, 2012). In this paper, we use the term bathymetry to refer to water depth, whereas other authors might use bathymetry to refer to bed elevations.

One of the longest-standing applications of remote sensing to rivers is estimation of water depth from passive optical image data, building upon the foundation established in marine environments. For example, early work by Lyzenga (1978) formed the basis for some of the first studies to explore the use of airborne multispectral image data for retrieving river depths (Lyon et al., 1992; Winterbottom & Gilvear, 1997). More recently, Legleiter (2013) showed that reasonable depth maps could be produced from aerial photographs publicly available through the National Agricultural Imagery Program. Similarly, the proliferation of high-resolution commercial satellites over the past 10–15 years has opened up the possibility of mapping river bathymetry from space (Legleiter & Overstreet, 2012). Because satellites can be readily tasked and provide images covering a greater spatial extent, this type of data is conducive to larger-scale investigations of long river segments or entire watersheds (e.g., Hugue et al., 2016). This capability is critical for realizing the "riverscape" vision articulated by Carbonneau et al. (2011) and understanding how, for example, various fish species utilize different portions of a river system throughout their life histories (Fausch et al., 2002). Dietrich (2016) explored the potential for this kind of valley-scale (tens of kilometers) riverscape mapping using remotely sensed data acquired from a helicopter. At the other end of the spectrum of spatial scales, UAS-based mapping has emerged as a convenient, economical means of characterizing channel morphology and in-stream habitat for short reaches, particularly with structure from motion (SFM) photogrammetric techniques that translate sequences of photographs into detailed, accurate digital elevation models (DEMs) and orthorectified images (e.g., Fonstad et al., 2013; Smith et al., 2016). Woodget et al. (2015) and Dietrich (2017) also have shown that data from UAS and SFM can provide reliable depth estimates in clear, shallow water. Finally, an alternative, active remote sensing approach to mapping river bathymetry involves newly developed airborne LiDAR systems equipped with green-wavelength lasers that, unlike standard NIR systems, can penetrate through the water column to the bed under certain conditions (e.g., Kinzel et al., 2013; Legleiter et al., 2016; McKean et al., 2008); Mandlburger et al. (2016) also reported initial results from a bathymetric LiDAR deployed from a UAS. Whereas previous studies primarily have examined small- to medium-sized, relatively shallow rivers, this paper evaluates the potential to estimate water depths in a larger channel, on the order of 100 m wide with depths in excess of 4 m, from various types of remotely sensed data.

In addition to the numerous sensors and platforms now available, a variety of algorithms have been developed for remote sensing of river bathymetry. For passive optical image data, depth retrieval requires establishing a relationship between reflectance and water depth. A traditional, still common approach involves relating georeferenced pixel values to colocated field-based depth measurements via regression (e.g., Winterbottom & Gilvear, 1997; Williams et al., 2014). Although this strategy is readily implemented, any regression-based method requires field observations from as close as possible to the time of image acquisition. The difficulty of coordinating ground-based and airborne data collection motivated the development of alternative techniques based on hydraulic principles (Fonstad & Marcus, 2005; Legleiter, 2015), probability concepts (Legleiter, 2016), or radiative transfer modeling (e.g., Kerr & Purkis, 2018). Another limitation of depth retrieval via simple linear regression is that the total at-sensor radiance depends not only on depth but also the reflectance of the streambed, the optical properties of the water column, and any light reflected from the water surface; atmospheric effects can further contaminate the radiance signal (Legleiter et al., 2004). As a result, depths inferred via regression can be influenced by any or all of these confounding factors, particularly variations in bottom reflectance.

A more robust approach attempts to account for these effects by evaluating band ratios as potential predictors of water depth. The Optimal Band Ratio Analysis (OBRA) method introduced by Legleiter et al. (2009) considers all possible band combinations and identifies the pair of wavelengths that provides the strongest relationship between an image-derived quantity, X, and flow depth, d. Initial testing and subsequent application of this approach demonstrated that OBRA yields reliable depth estimates in the presence of variable substrates, water column characteristics, and water surface textures (Legleiter et al., 2009, 2011, 2016). This type of spectrally based remote sensing, however, is only feasible under certain, fairly restrictive conditions:

The water must be clear and relatively shallow, and the channel must be visible from above, unobstructed by riparian vegetation or shadows. Although originally designed for continuous field spectra or hyperspectral image data, which allow wavelengths highly sensitive to variations in depth to be identified and exploited, OBRA also has been applied successfully to aerial photographs and multispectral satellite images with fewer, broader bands (Legleiter & Overstreet, 2012; Legleiter, 2013).

More recently, Legleiter et al. (2018) introduced an iterative version of the algorithm, called OBRA of Progressively Truncated Input Depths (OPTID), intended to further optimize the X versus d relation by limiting the range of depths used for calibration. By taking subsets of the original field data, OPTID aims to construct a calibration data set conducive to accurate depth retrieval. Although this type of sampling is an important aspect of the overall calibration process, improving the model selection and curve-fitting components of this process also could yield more reliable depth maps. For example, Legleiter et al. (2009) observed that using a linear X versus d relation can lead to negative depth estimates along shallow channel margins and under-predictions of depth in pools. Following Dierssen et al. (2003), Legleiter and Overstreet (2012) showed that incorporating an X^2 term in the regression could improve depth retrieval in deeper areas, but Legleiter et al. (2018) pointed out that quadratic OBRA can lead to minimum image-derived depths greater than the shallowest depths observed in the field. Considering alternative functional forms for the X versus d relation could mitigate these issues and thus enable more accurate depth retrieval across the full range of depths present in the river of interest. In this study, we generalize the OBRA framework by considering linear, quadratic, exponential, and power models, as well as a scatter plot smoothing technique known as lowess (Cleveland & Devlin, 1988; Dilbone et al., 2018). We also apply a nonparametric machine learning technique known as K nearest neighbors regression (KNN; Kibele & Shears, 2016) and compare these passive optical techniques to a bathymetric LiDAR instrument. Finally, by reporting in situ measurements of water column optical properties from our field site on the Sacramento River, we provide a quantitative, physical basis for understanding a key constraint on remote sensing of river bathymetry: the maximum depth detectable by a particular sensor.

Interest in remote sensing of rivers continues to increase, with an expanding user community that now encompasses not only academic researchers but also agency scientists and resource management professionals. As applications of this new technology become more widespread, information on the relative merits and limitations of various approaches is critical to ensuring efficient, cost-effective use of remote sensing. In keeping with our overall goal to advance fluvial remote sensing by developing and testing new techniques for bathymetric mapping, this study focused on the following research objectives:

1. Make field measurements of water column optical properties and compare observations from the Sacramento River to data from other sites to establish a physical foundation for understanding controls on depth retrieval performance.
2. Introduce a new version of OBRA that generalizes the calibration process by considering several functional forms for describing the relationship between the image-derived quantity X and the flow depth d: linear, quadratic, exponential, power, and lowess models; we also apply a nonparametric KNN technique to infer depths from image data.
3. Evaluate the potential to measure the bathymetry of a large gravel-bed river via multiple remote sensing approaches, including multispectral satellite images, hyperspectral data acquired from manned aircraft and UAS, and water-penetrating green LiDAR.
4. Quantify depth retrieval performance across a range of depths by examining the distribution of depth retrieval errors spatially and as a function of depth and by performing generalized OPTID.

2. Methods

2.1. Study Area and Field Data Collection

The Sacramento River is located in California's Central Valley and is the state's largest river, with a drainage area of 6.8×10^4 km^2. The river is a vital source of water for urban and agricultural uses and supports three runs (populations) of Pacific salmon listed under the Endangered Species Act (Moyle et al., 2017). Flow in the upper Sacramento is regulated by Shasta and Keswick Dams and the mean annual discharge measured at the U.S. Geological Survey (USGS) gage (11377100) near Red Bluff, CA, since dam closure in 1964 has been 357 m^3/s. These two dams are migration barriers for salmon and prevent access to historical habitat in upstream cold-water tributaries. As a result, salmon now spawn and rear in the reaches downstream of Keswick Dam and dam releases must meet a range of water management requirements. Several decision

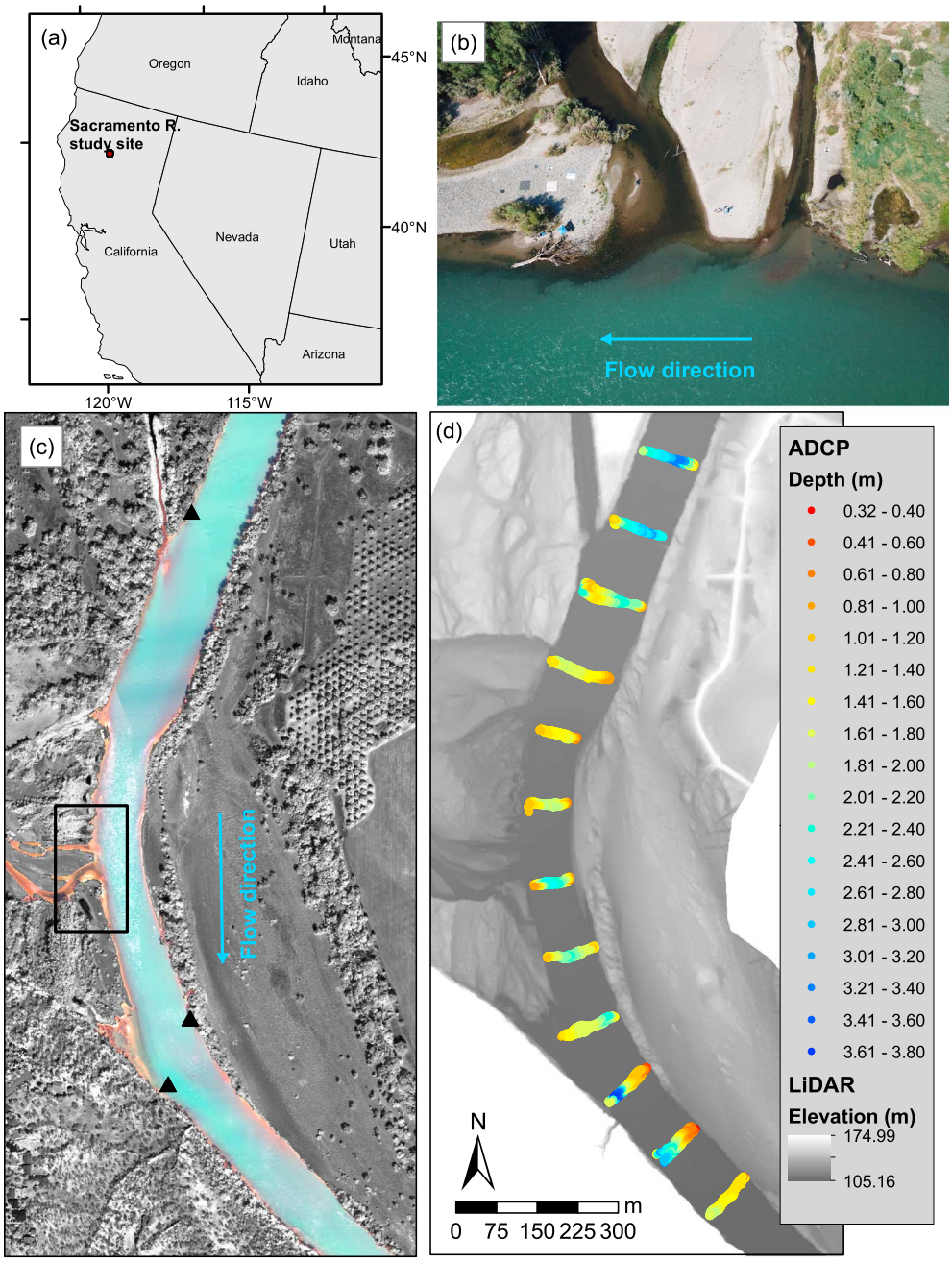

Figure 1. (a) Location of the upper Sacramento River in northern California, USA. (b) Image of the study reach at the Cottonwood Creek confluence acquired from a small unmanned aircraft system, courtesy of Alicia Amerson of AliMoSphere. (c) Compact Airborne Spectrographic Imager hyperspectral image with terrestrial areas represented in grayscale using a near-infrared band (744 nm) and the in-stream portion of the image displayed as a color composite with bands centered at 687, 573, and 473 nm as red, green, and blue, respectively. The black triangle symbols overlain on the image represent the location of field measurements of water column optical properties, and the rectangle indicates the location of the image shown in (b). (d) Near-infrared LiDAR topography with hydroflattened water-surface elevations overlain by field-based depth measurements from 12 ADCP/echo sounder cross sections. ADCP = acoustic Doppler current profiler.

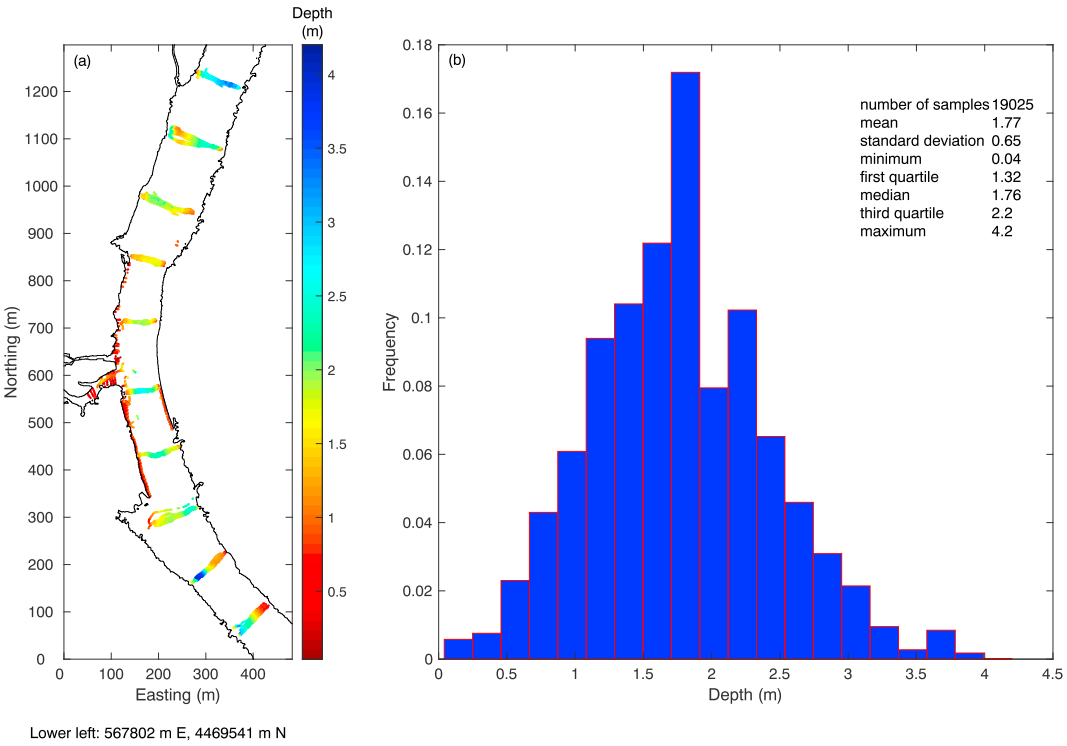

Figure 2. (a) Map of field-based depth measurements made by wading shallow channel margins and deploying an acoustic Doppler current profiler and echo sounder from a jet boat along multiple passes of the 10 cross sections encompassed by the unmanned aircraft system-based hyperspectral image. (b) Histogram and summary statistics for the composite, cross-calibrated depth data set.

support tools have been developed to optimize these complex water operations, including coupled models of flow and water temperature (Danner et al., 2012; Pike et al., 2013) and salmon bioenergetics (Dudley, 2018). These tools require accurate river bathymetry, which to date has been surveyed using boat-based hydroacoustic methods with a mean cross-section spacing of approximately 500 m (Pike et al., 2013). Ongoing efforts to evaluate in-stream habitat conditions and identify restoration targets on the Sacramento rely upon high-resolution topo-bathymetric data, creating a compelling need to evaluate various approaches for remote sensing of river bathymetry.

To pursue this objective and facilitate a large-scale habitat inventory for winter-run Chinook salmon, remotely sensed data were acquired for approximately 112 km of the upper Sacramento near the city of Redding, California. In this study we focused on a 1.6-km reach centered on the confluence with Cottonwood Creek (Figure 1a). Located in an agricultural landscape with riparian forest adjacent to the channel, this reach has a gravel bed, a slope of 0.00097, a mean wetted width of 111 m, and a mean depth of 1.8 m. The study area features a single, large meander bend, with Cottonwood Creek entering from the right bank (i.e., from the west) near the apex and a bluff rising above the river as the channel curves to the left. Field data collection and acquisition of remotely sensed data occurred under base flow conditions; the discharge measured 21 km downstream at USGS gaging station 11377100 remained steady at 270 m^3/s throughout September 2017, when the airborne and UAS-based and hyperspectral images and bathymetric LiDAR were collected. The discharge dropped to 237 m^3/s before the satellite image data were acquired on 18 October, but this reduction in flow would have produced only a minor decrease in depth. The Sacramento River was slightly turbid during the study, with a pale green color, whereas the small amount of water in Cottonwood Creek was very clear and appeared much darker at the confluence of the two streams (Figures 1b and 1c).

The various data sets used in this study are available from the USGS ScienceBase catalog via a landing page with links to seven individual data releases (Legleiter & Harrison, 2018). Only a brief overview of our field methods is provided here but additional detail is included in the metadata associated with each data release. We collected field-based depth measurements from a jet boat and by wading. The wading surveys involved using real-time kinematic (RTK) GPS receivers to record water-surface elevations (WSEs) along the edge of

the channel and bed elevations in shallow areas safely accessible from the bank; depths were calculated by subtracting each bed elevation measurement from the nearest WSE point. These depth measurements were obtained by recording WSE points every 2–5 m along the water's edge and then wading out into the channel to survey an additional 5–15 bed elevations. The field measurements of WSE did not cover the entire reach and were used only for calculating depths from the wading surveys in shallow areas, not for deriving depth information from LiDAR data, as described below.

For the more extensive, deeper portions of the channel, we used the boat to survey 12 cross sections spaced approximately every 135 m along the river (Figure 2a), making 5–10 passes back and forth across the channel at each cross section. Ten of these cross sections were encompassed by the UAS-based hyperspectral image, the remotely sensed data set with the smallest spatial extent, and we only used data from this subset of the field survey. Depths were recorded using two different instruments: an acoustic Doppler current profiler (ADCP) and a single-beam echo sounder. Each sensor made a measurement once per second as the boat traversed the channel, resulting in a mean point density of 17.56 points per meter of distance along a cross section, with a range from 10.62 to 23.20 points per meter among the 10 cross sections. The spatial locations of the depth measurements were obtained with a differential GPS included as part of the ADCP instrument package, which provided a spatial accuracy on the order of 15–20 cm, and with an RTK GPS receiver coupled to the echo sounder, which provided a typical spatial accuracy of 2–3 cm. To ensure consistency between the two instruments, the ADCP- and echo sounder-based depth measurements were cross-calibrated using points that were located within a distance of 0.5 m of one another. We quantified the error associated with these depth measurements by calculating the standard deviation of the depths recorded at all other points within 0.5 m of each individual point. These depth standard deviations averaged 0.037 ± 0.034 m (mean $\pm$ standard deviation) over the 10 cross sections, implying that depth measurement errors were typically less than 4 cm. The resulting, composite (i.e., wading-based and boat-based) data set consisted of over 19,000 individual depth measurements and was approximately normally distributed with mean and maximum depths of 1.77 and 4.2 m (Figure 2b). We used the original depth measurement points for calibration and validation of remotely sensed depth estimates rather than producing a continuous, gridded surface representation to avoid introducing any additional uncertainty associated with interpolating a bathymetry (Conner & Tonina, 2014; Glenn et al., 2016).

Optical properties of the water column exert a primary control on the feasibility of mapping river bathymetry via remote sensing and are influenced by suspended and dissolved constituents such as sediment and organic matter. More specifically, the physical foundation for estimating water depth from various kinds of remotely sensed data is the attenuation of light with distance traveled through the water column, whether the light originates from the sun for passive optical images or from a laser for LiDAR. To better understand how radiative transfer processes influence depth retrieval performance across a range of river environments, we collected field data on water column optical properties from our study area on the upper Sacramento and compared these measurements with similar data sets from six other streams where remote sensing investigations have been performed: the Deschutes River in Oregon (Legleiter et al., 2018), the Niobrara River in Nebraska (Dilbone et al., 2018), the Snake River in Wyoming, and the Colorado and Blue Rivers and Muddy Creek at their mutual confluence in Colorado (Legleiter et al., 2016).

To quantify radiative transfer processes independent of illumination and viewing geometry, we used a WET Labs ac-s to measure two inherent optical properties (IOPs): the beam absorption and beam attenuation coefficients $a(\lambda)$ and $c(\lambda)$, where λ denotes wavelength. These data consist of 81 contiguous bands spanning the region from 400 to 747 nm with a 4-nm sampling interval. The attenuation so critical for depth retrieval is the combined result not only of absorption but also scattering of light. This concept is expressed mathematically as $c(\lambda) = a(\lambda) + b(\lambda)$, where the scattering coefficient $b(\lambda)$ can be further decomposed into a backscattering coefficient $b_b(\lambda)$ that describes radiation redirected into the hemisphere from which the incident beam approached (i.e., back toward the detector in a remote sensing context). This scattered light imparts a volume reflectance to the water column itself and thus defines a river's color and level of turbidity. We used a WET Labs EcoTriplet to measure the backscattering coefficient b_b at a single wavelength (700 nm). The same basic measurement also was used to obtain values of turbidity, a more common metric of water clarity that is not a true IOP but is widely used in monitoring programs (Davies-Colley & Smith, 2001). In addition, the EcoTriplet measured the concentrations of two optically significant constituents of the water column: chlorophyll and colored dissolved organic matter. Another key constituent is suspended sediment, the concentration and particle size of which we measured with a Sequoia Scientific LISST 100-X;

Table 1
Summary of Remotely Sensed Data Sets

Acquisition dates	Data type	Sensor	Height (km)	Pixel size (m)	Bands	Wavelength(s) (nm)
18 Oct. 2017	Satellite multispectral	WorldView-3	617	1.36	8	400–954
13 and 15 Sep. 2017	Airborne hyperspectral	CASI 1500H	1	0.5	48	373–1,043
13 Sep. 2017	UAS-based hyperspectral	Nano-Hyperspec	0.12	0.18	276	396–1,005
10–17 Sep. 2017	Bathymetric LiDAR	Riegl VQ-880-G	0.4	0.4	1	532

Note. CASI = Compact Airborne Spectrographic Imager; UAS = unmanned aircraft system.

we used the median particle diameter D_{50} to summarize the grain size distribution. All three instruments (ac-s, EcoTriplet, and LISST) were deployed by lowering them from the boat into the water until submerged by approximately 0.5 m, sampling for three minutes, and then computing a time average for each optical quantity. To account for any potential, minor influence of the small tributary entering the Sacramento River within our study reach, these optical field measurements were made at three different locations (above the Cottonwood Creek confluence near the right bank and below the confluence near each bank of the Sacramento; Figure 1c) and then averaged to obtain representative values for the reach as a whole.

2.2. Remotely Sensed Data and Image Processing

We evaluated the potential to map river bathymetry with a range of different sensors deployed from a variety of platforms by considering four distinct remotely sensed data sets (Table 1), also accessible from the USGS ScienceBase (Legleiter & Harrison, 2018). The most readily available type of data was a multispectral image acquired by the WorldView-3 (WV3) satellite. This instrument measures radiance in eight visible and NIR bands, including coastal and yellow channels specifically intended for water-oriented applications. The original image used in this study was only approximately georeferenced and did not align closely with our ground-based surveys. We used ArcMap software tools, a 10-m DEM from the USGS National Elevation Dataset, and information on satellite viewing geometry provided along with the image to perform orthorectification with a rational polynomial coefficient model. This process greatly improved coregistration with our field data, such that all of our survey points were located within the channel as depicted in the image. To assess the impacts of varying levels of radiometric preprocessing on depth retrieval performance, we analyzed three different versions of the orthorectified WV3 image: (1) raw data consisting of uncalibrated digital numbers, (2) top-of-atmosphere reflectances calculated following Kuester (2016), and (3) apparent surface reflectances derived using the Quick Atmospheric Correction algorithm developed by Bernstein et al. (2012) and included in the ENVI software package.

Hyperspectral scanners measure radiance in a larger number of narrower spectral bands and could enhance bathymetric mapping by taking advantage of specific wavelengths that are highly responsive to changes in depth. To examine this possibility, we collected hyperspectral images from both a fixed-wing, manned aircraft and a small unmanned aircraft system (UAS); we refer to the two data sets as airborne hyperspectral and UAS-based hyperspectral. The airborne data were acquired with a Compact Airborne Spectrographic Imager (CASI) 1500H (Innovation, Technology, Research, Excellence, and Science (ITRES), 2014) deployed on a Cessna Caravan. This pushbroom sensor features an adjustable band configuration, and for this study we acquired 48 bands with a 0.5-m pixel size. The raw CASI data were radiometrically calibrated and ATCOR-4 atmospheric correction software (ReSe, 2014) used to produce an image in units of apparent surface reflectance. Direct georeferencing based on data recorded by a GPS and inertial motion unit onboard the aircraft during the flight provided accurate, pixel-scale image coregistration with surveyed ground control targets used as checkpoints.

The UAS-based hyperspectral image was acquired from a DJI Matrice 600 multirotor UAS equipped with a compact, lightweight Nano-Hyperspec imaging system (Headwall Photonics, 2018), which we refer to as the Nano. Because this instrument is a line scanner, two-dimensional spatial images can only be obtained through motion of the platform. Due to the Nano's relatively narrow 640-pixel swath width and regulations on UAS flying height, complete coverage of the Sacramento River required several parallel, along-channel flight lines. All of these lines were acquired while flying in the same direction to avoid inconsistencies related to the effects of viewing and illumination geometry on reflectance from the water surface (Legleiter et al., 2017). Raw Nano images were georeferenced using postprocessed kinematic GPS and inertial motion unit

data recorded onboard the UAS and individual flight lines were combined into an orthorectified mosaic. Additional preprocessing involved applying calibration coefficients to convert digital numbers to radiance and then using a calibration tarp placed on the ground before the flights as an in-scene white reference to produce a final reflectance image. Because this image was derived from a sequence of scan lines rather than instantaneous, full-frame images, the Nano data were not suitable for the bathymetric SFM techniques described by Woodget et al. (2015) and Dietrich (2017).

The same image processing steps were applied to the satellite, airborne, and UAS-based data sets. This workflow involved defining a channel mask using a NIR band threshold, manually editing the initial mask as needed, and then smoothing the in-stream portion of each image with a spatial filter. We used our field-based depth measurements to calculate pixel-scale mean depths by assigning each point to the closest pixel center and then averaging all of the depth measurements assigned to a given pixel. Image spectra were extracted from these locations and the resulting paired observations of depth and reflectance served as input to the various depth retrieval algorithms described below.

In addition to these passive optical imaging systems, we also evaluated the bathymetric mapping capabilities of the VQ-880-G LiDAR (Riegl, 2018). This sensor was deployed from the same Cessna Caravan as the CASI, but at a lower flying height that yielded a laser pulse footprint diameter of 0.4 m (Table 1). The VQ-880-G features both a water-penetrating green (532 nm) laser capable of measuring submerged bed elevations under certain conditions and a NIR laser (1,064 nm) used to assist in modeling the water surface. The system records the full waveform for each emitted laser pulse and thus enables range measurements for all discernible targets for a given pulse. Additional detail on the acquisition and processing of the LiDAR data are available in the technical report provided by the flight contractor and included with our data release (Legleiter & Harrison, 2018); only a brief summary is provided here. Processing tasks included GPS control computations, deriving a smoothed best estimate of the aircraft trajectory, applying kinematic corrections, calculating laser point positions, and classifying the LiDAR point cloud. Points classified as ground were used to test relative accuracy by comparing adjacent flight lines and to perform automated line-to-line calibrations that accounted for any variation in system attitude parameters; the resulting corrections were applied to all points within a given flight line. Riegl's RiProcess software was used to identify and process bathymetric returns from the channel bed, which included applying a refraction correction based on the local WSE and the laser's angle of incidence. The number of bottom returns identified via automated and manual classification methods can be limited by the depth and turbidity of the water column and by the reflectance of the streambed; McKean et al. (2014) provide a thorough discussion of the many complications and sources of error associated with bathymetric LiDAR data. In this study, areas lacking bottom returns were excluded from topo-bathymetric DEM's and explicitly flagged as “no data” voids.

2.3. Depth Retrieval Algorithms

2.3.1. OBRA

In addition to different sensors and platforms, we also considered various methods of inferring water depths from remotely sensed data. For the passive optical images, we focused on OBRA (Legleiter et al., 2009). This method uses ratios of spectral bands to isolate the effect of depth on the total at-sensor radiance while accounting for the confounding influence of variations in bottom reflectance, water column optical properties, and reflectance from the water surface. More specifically, the image-derived quantity X is defined as

$$X = \ln\left[\frac{R(\lambda_1)}{R(\lambda_2)}\right], \tag{1}$$

where $R(\lambda_1)$ and $R(\lambda_2)$ are reflectances, radiances, or raw digital numbers recorded in the numerator and denominator bands centered at wavelengths λ_1 and λ_2, respectively. The OBRA algorithm takes as input paired observations of depth d and the radiometric quantity $R(\lambda)$, calculates X values for all possible band combinations, and regresses X against d for each version of X. The optimal band ratio is taken to be that (λ_1, λ_2) pair that yields the highest coefficient of determination R^2.

2.3.2. Generalized OBRA

In this study, we generalized the OBRA framework by considering several functional forms to enable more flexible curve-fitting in calibrating X to d. More specifically, generalized OBRA (GenOBRA) involves

developing X versus d relations for four different types of equations. The simplest model is the linear expression

$$d = b_0 + b_1 X, \tag{2}$$

where b_0 and b_1 are the the intercept and slope of the best fit regression line. A quadratic model is defined similarly as

$$d = b_0 + b_1 X + b_2 X^2, \tag{3}$$

with an additional coefficient b_2 for the quadratic term. The first new functional form introduced as part of GenOBRA is an exponential equation given by

$$d = b_0 e^{b_1 X}, \tag{4}$$

where b_0 is a multiplicative coefficient and b_1 is a multiplier on X in the exponential term. Equation (4) can be linearized for regression purposes as

$$\ln(d) = ln(b_0) + b_1 X, \tag{5}$$

such that the slope of the best fit line on a plot of X versus $\ln(d)$ is equal to b_1 and b_0 is obtained by raising e to the intercept of the regression line. Similarly, the second new function in GenOBRA is the power model

$$d = b_0 X^{b_1}, \tag{6}$$

where b_1 now represents the power to which X is raised. Again, this expression can be linearized to facilitate regressions of the form

$$\ln(d) = ln(b_0) + b_1 \ln(X). \tag{7}$$

In this case, the slope of the best fit line on a plot of $\ln(X)$ against $\ln(d)$ is the exponent b_1, and the coefficient b_0 is again derived by raising e to the intercept of the line.

2.3.3. Lowess OBRA

In addition to these four functional forms, we also evaluated another curve-fitting option, a locally weighted linear regression technique called lowess. Dilbone et al. (2018) explored lowess-based calibration of X to d as a means of avoiding spurious overestimates of water depth along shallow channel margins. Lowess is shorthand for "locally weighted scatter plot smooth" and involves using first-order polynomials to fit a trend line through noisy data. We used a routine based on the MATLAB function "smooth" and set the span to 20% of the total number of data points. Technically, lowess is not intended for prediction, but we adapted the method for this purpose by using the data points on an (X, d) scatter plot to interpolate a value of d for any value of X not present in the calibration data set or to linearly extrapolate an estimate of d for any X outside the range of X values available for calibration.

2.3.4. Generalized OPTID

Another recent refinement of OBRA involves applying the algorithm iteratively to different subsets of the calibration data created by excluding observations that exceed a series of specified cutoff depths. This method, deemed OPTID, is intended to optimize the process of calibrating X to d by removing data that exceed the maximum depth, denoted by d_{max}, a particular sensor can detect in the river of interest. This approach thus provides information on depth retrieval performance across various ranges of depths and could be used to infer d_{max} directly from an image rather than via theoretical calculations based on field measurements of water column optical properties (Legleiter & Overstreet, 2012; Mishra et al., 2005; Philpot, 1989). Legleiter et al. (2018) hypothesized that an inflection point on a plot of OBRA R^2 versus cutoff depth could be interpreted as an indication of d_{max}. In this study, we generalized OPTID by incorporating linear, exponential, and power X versus d relations into the iterative procedure, in addition to the quadratic version of OBRA as in Legleiter et al. (2018). We performed generalized OPTID for field spectra and three different types of passive optical image data with a 0.05-m increment between cutoff depths, starting from 0.5 m and increasing to 3 m for the field spectra and 3.8 m for the images.

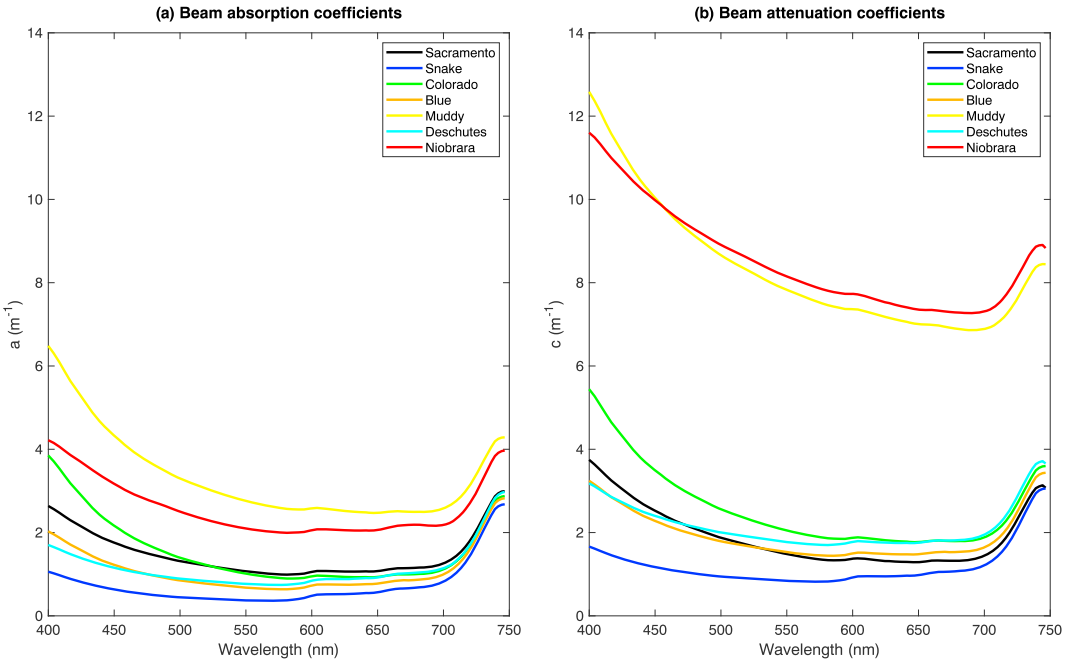

Figure 3. Field measurements of absorption and attenuation from our study site on the Sacramento River and six other streams where similar data sets were acquired during previous remote sensing investigations (see text for details). Beam absorption coefficients $a(\lambda)$ are plotted in (a) and beam attenuation coefficients $c(\lambda)$ are plotted in (b) using the same axis limits for comparison.

2.3.5. KNN

As an alternative to OBRA-based depth retrieval, we also considered a nonparametric machine learning technique called KNN. KNN is designed to estimate a continuous response variable based on the K nearest training samples in a multivariate feature space, without making any assumptions regarding the distribution or linearity of the data. In the present context, the unknown depth $\hat{d}$ is predicted based on the spectrum, denoted by the vector $\mathbf{R}'$, extracted from the image at that location by averaging the values of the K pixels with known depths d and reflectances $\mathbf{R}$ that are closest to $\mathbf{R}'$ in spectral feature space. The depth estimate is given by

$$\hat{d} = \frac{1}{K}\sum_{i=1}^{K} d_i, \tag{8}$$

where in this study we used the $K = 5$ nearest values of d based on the Euclidean distance l between $\mathbf{R}'$ and each of the training pixels. This distance metric is calculated as

$$l(\mathbf{R}, \mathbf{R}') = \sqrt{\sum_{i=1}^{n} (R_i - R_i')^2}, \tag{9}$$

where i indexes the n spectral bands. In summary, given paired observations of depth and reflectance, KNN estimates unknown depths as the mean of the $K = 5$ nearest (in terms of reflectance across all bands) pixels with known depths; all estimated depths thus fall within the range of depths included in the calibration data set (Kibele & Shears, 2016).

2.3.6. Calculating Depth From Bathymetric LiDAR Data

The bathymetric LiDAR data were provided as bed elevations rather than depths and thus were not directly comparable to depths estimated from passive optical images. To enable such a comparison, we calculated depths from the LiDAR by subtracting bed elevations from a WSE model derived from NIR LiDAR acquired at the same time as the bathymetric (green) LiDAR. The water surface model was generated using NIR returns within breaklines defining the water's edge. The NIR water surface points were filtered and edited by the flight contractor to obtain the most accurate representation of the water surface, which was modeled as a triangulated irregular network. Evaluation of 26 wetted edge checkpoints by the contractor resulted

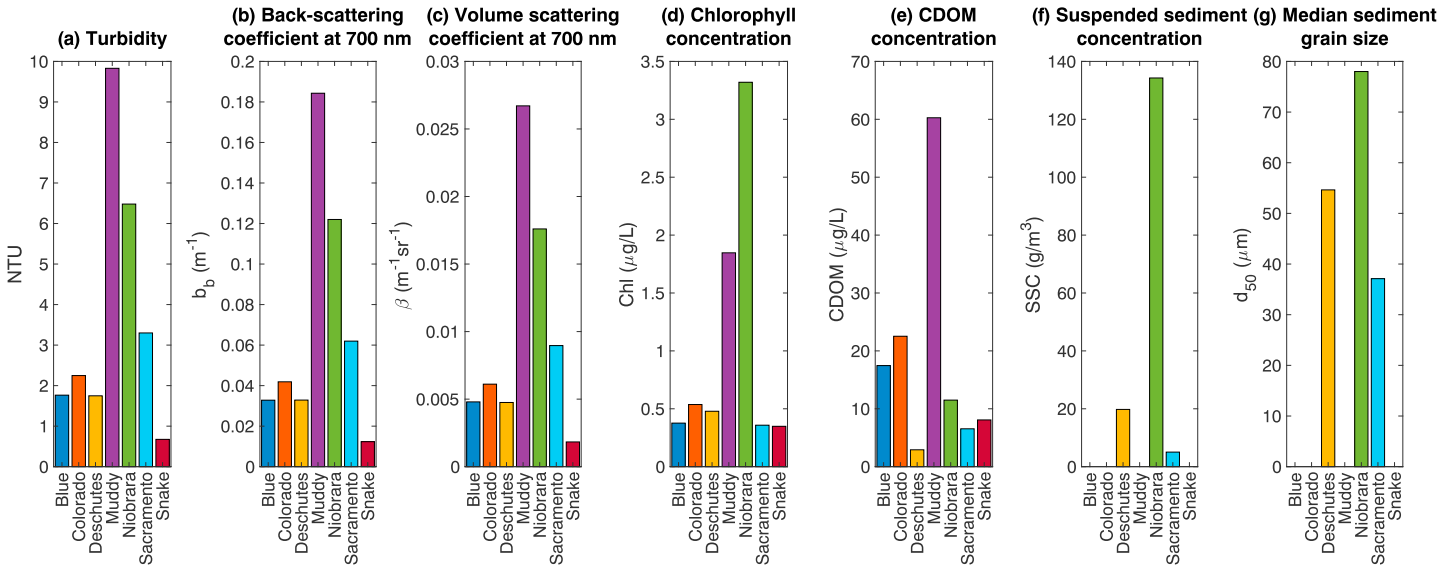

Figure 4. Field measurements of water column optical properties and concentrations of optically significant constituents from the Sacramento River and six other sites with similar field data sets (see text). Field data on (f) suspended sediment concentration and (g) median sediment grain size were not available for the Blue River, Colorado River, Muddy Creek, and Snake River. The same bar colors are used in all panels and used only to distinguish among sites, not to represent water clarity. NTU = Nephelometric Turbidity Units.

in a mean vertical accuracy of −0.033 m with a standard deviation of 0.043 m; a more detailed accuracy assessment is provided in the report included with the LiDAR data release (Legleiter & Harrison, 2018). These results imply that the accuracy of the LiDAR-derived water surface was not a limiting factor in our analysis.

Areas with insufficient or no bottom returns from the green laser were identified by triangulating bathymetric points with a maximum edge length of 4.56 m to ensure that any area greater than 9 m^2 was flagged as a data void. Depths were not calculated for these areas.

2.4. Performance Assessment

To quantify the bathymetric mapping capabilities of various sensors, platforms, and algorithms, we used several different metrics of depth retrieval performance. For GenOBRA, the OBRA R^2 value for the optimal band ratio provided an indication of the strength of the relationship between the image-derived quantity X, defined using equations (2), (3), (4), or (6), or via lowess, and field measurements of flow depth d, based on the paired observations of depth and reflectance available for calibration. The same 5% sample of the original field data was used to calibrate all algorithms, with the remaining 95% set aside to assess the accuracy of depths estimated from remotely sensed data by OBRA, KNN, or LiDAR. This validation involved performing observed vs. predicted (OP) regressions (Pineiro et al., 2008). The OP R^2 value quantifies agreement between field observations and depths predicted via remote sensing, while the intercept and slope coefficients of the OP regression provide information on the bias associated with these estimates. For an ideal depth retrieval approach, the OP regression would coincide with the 1-to-1 line, resulting in an OP R^2 of 1; a slope of 1 and intercept of 0 would indicate unbiased estimates.

In addition to the OBRA and OP regression analyses, we also used the validation subset of the field data to quantify the accuracy and precision of the various remotely sensed bathymetries. More specifically, for each validation point, we calculated the depth retrieval error ε as the difference between the field measurement of depth d_f and the depth estimated via remote sensing d_r:

$$\varepsilon = d_f - d_r. \tag{10}$$

Positive values of ε thus imply that the remotely sensed depth was shallower than that measured in the field (i.e., an underprediction of depth) and conversely a negative ε indicates that the remotely sensed depth was greater than the field measurement (i.e., an overprediction of depth). For each combination of sensor, platform, and algorithm, we calculated depth retrieval error summary statistics; the mean error served as an

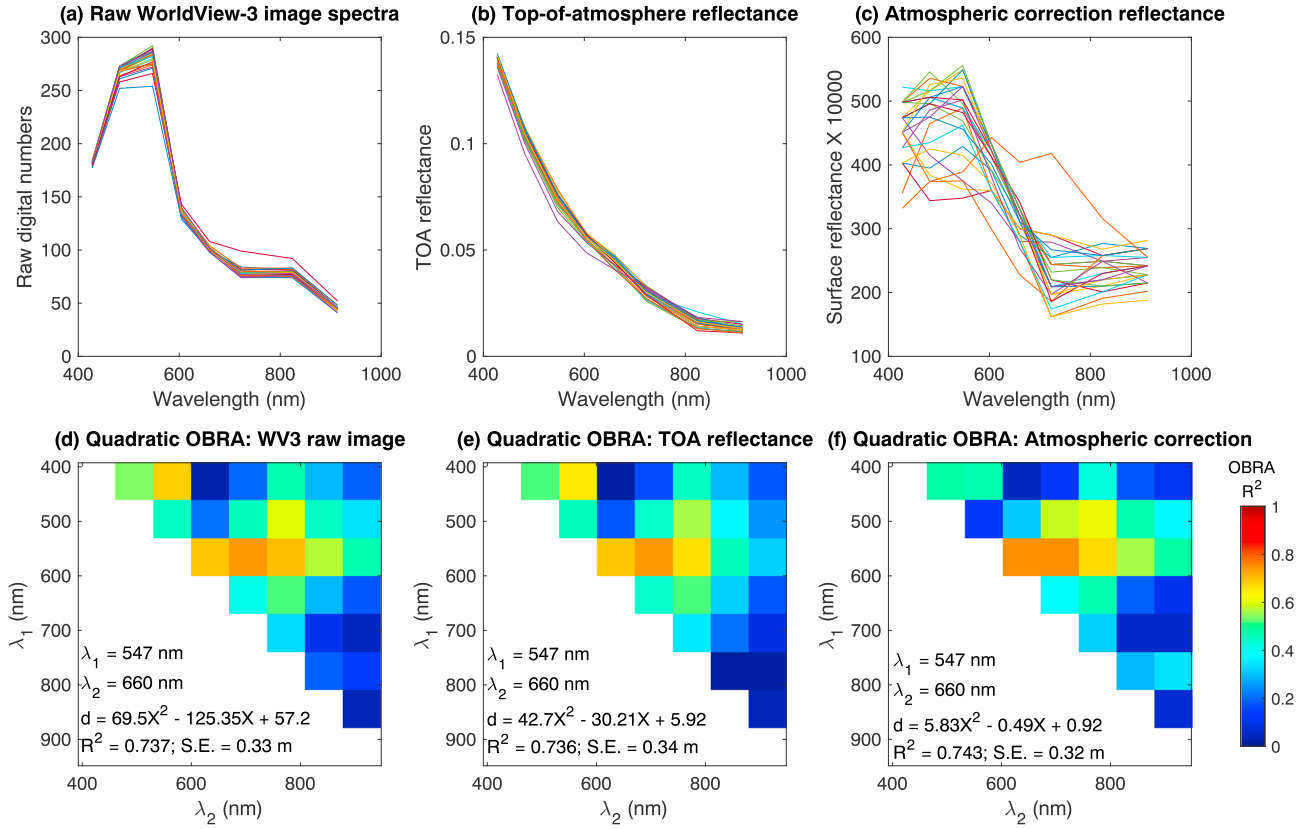

Figure 5. (a–c) Example spectra and (d–f) quadratic OBRA matrices for basic, TOA reflectance, and atmospherically corrected versions of the WV3 satellite image. The spectra plotted in (a)–(c) were selected at random from the in-stream portion of each version of the WV3 image and different line colors were used only to distinguish among the individual spectra. OBRA = Optimal Band Ratio Analysis; TOA = top-of-atmosphere; WV3 = WorldView-3.

indication of bias (i.e., underprediction or overprediction of depth, on average) and the standard deviation of ε provided an index of precision. We also used box plots to compare distributions of ε for the various approaches. Similarly, to illustrate how bathymetric accuracy varied as a function of depth, we plotted ε versus d; ideally, such a plot would not exhibit any obvious trend, with a random, normal distribution about the horizontal axis. Finally, to visualize the spatial pattern of depth retrieval errors in the context of channel morphology, we produced error maps by plotting ε values at the location of the corresponding validation points.

3. Results

3.1. Water Column Optical Properties

Figure 3 summarizes our field measurements of absorption and attenuation from the Sacramento and places them in the context of the other rivers. In all cases, the beam absorption and attenuation coefficients $a(\lambda)$ and $c(\lambda)$ were highest at shorter blue wavelengths due to chlorophyll and organic matter dissolved within the water column. $a(\lambda)$ and $c(\lambda)$ declined with wavelength into the green, stabilized around 575 nm, and then increased abruptly beyond 700 nm due to strong absorption of NIR radiation by pure water. In comparison with the other sites, the Sacramento had intermediate IOP's, with values of $a(\lambda)$ and $c(\lambda)$ that were much lower than the sediment-laden Muddy Creek and Niobrara River but higher than the clear-flowing Snake River.

Consistent with our qualitative field observations of the Sacramento's bluish-green hue and moderate water clarity, the EcoTriplet data summarized in Figures 4a and 4b indicate that the Sacramento had turbidity and $b_b(700)$ values in between the visually opaque Muddy and Niobrara sites and the other, relatively clear streams. The measured amounts of organic matter within the Sacramento River were relatively small, however, with a chlorophyll concentration nearly as low as the oligotrophic Snake River and a colored dissolved organic matter (CDOM) concentration lower than every other river except for the Deschutes

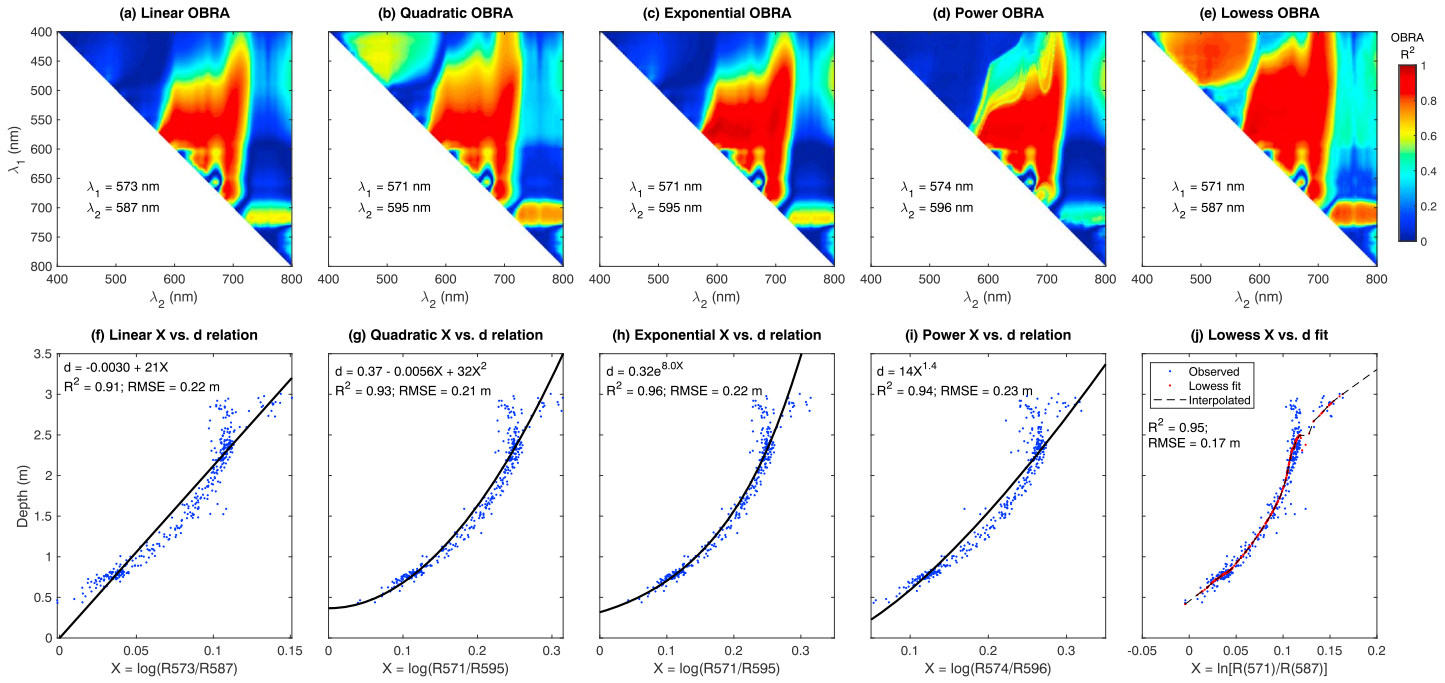

Figure 6. Generalized OBRA output for field spectra measured along the Sacramento River. (a–e) OBRA matrices illustrating spectral variations in the strength of the relationship between the image-derived quantity X and flow depth d modeled using (a) linear, (b) quadratic, (c) exponential, (d) power, and (e) lowess functions. (f–j) Corresponding X versus d calibration scatter plots for each type of model. Analogous figures for each of the passive optical image data sets evaluated in this study are provided as supporting information (Figures S1–S3). OBRA = Optimal Band Ratio Analysis; RMSE = root-mean-square error.

(Figures 4c and 4d). Suspended sediment also influences water column IOP's, but LISST measurements of sediment concentration and particle size were only available for three of the sites in our current database (Figures 4e and 4f). Relative to the Deschutes and Niobrara Rivers, the upper Sacramento had lower concentrations of finer-grained sediment, leading to greater water clarity on the Sacramento.

3.2. Preprocessing of Multispectral Satellite Image Data

Of the various remotely sensed data sets we evaluated, the most widely available was the multispectral image acquired by the WV3 satellite. DigitalGlobe provides a number of data products with different levels of preprocessing, but the basic deliverable consists of an image with pixel values in raw digital counts. Example spectra extracted from within the Sacramento River channel for this type of raw image are shown in Figure 5a but were difficult to interpret because they had not been converted to physically meaningful radiometric units. DigitalGlobe has published coefficients for performing such a radiometric calibration and Kuester (2016) provided instructions for calculating top-of-atmosphere (TOA) reflectances. These calculations account for sensor characteristics and variations in the amount of incident solar energy, which depend on location, time of year, and time of day and thus provides a means of standardizing images from different places and dates. The effects due to Earth's atmosphere will remain, however. The example spectra shown in Figure 5b illustrate the strong influence of atmospheric scattering, which is most pronounced at shorter blue wavelengths, on TOA reflectances, particularly for a relatively dark target like water. Differences among the spectra in Figure 5b are dwarfed by the atmospheric effects expressed as a much more significant decrease in TOA reflectance from nearly 0.15 to 0.01 with increasing wavelength across the eight WV3 bands. A more rigorous approach to image normalization thus would involve some form of atmospheric correction; we used the Quick Atmospheric Correction model (Bernstein et al., 2012) to produce an apparent surface reflectance image consisting of in-stream spectra like those shown in Figure 5c. This more advanced degree of processing lead to individual spectra that were much more distinct from one another, with reflectances varying from approximately 0.015 to 0.06, and therefore potentially more useful for depth retrieval.

To assess the impact of these three levels of radiometric preprocessing—essentially none, TOA reflectance, and full atmospheric correction—on the feasibility of mapping river bathymetry from WV3 satellite data, we performed quadratic OBRA for each version of the Sacramento River image; a quadratic function was selected because this type of model has proven effective in previous applications of OBRA and was readily implemented within our standard, existing workflow. The results of this analysis are summarized in Figures 5d–5f. The OBRA matrices for the three image variants were very similar to one another and in all cases the optimal band ratio consisted of an identical green numerator and a red denominator. More importantly, the OBRA calibration R^2 values were nearly identical across the three images, indicating that the relationship between the image-derived quantity X and flow depth d was just as strong for the original, raw image as for the version processed to mitigate atmospheric effects. Based on these results, we only used the original WV3 image rather than the TOA reflectance or atmospherically corrected versions that did not appreciably improve depth retrieval, in making comparisons among different sensors and algorithms.

3.3. GenOBRA

Although OBRA has proven to be an effective means of estimating flow depths from various passive optical image data sets across a range of river environments, we hypothesized that this approach could be further enhanced by generalizing the curve-fitting phase of the calibration process. In this study, we considered not only the linear and quadratic X versus d relations used in previous applications of OBRA but also introduced new exponential, power, and lowess models. To evaluate whether and to what extent each functional form could improve depth retrieval for various kinds of data, we performed GenOBRA for continuous field spectra, a multispectral satellite image, and airborne and UAS-based hyperspectral images of the upper Sacramento River. The results of this analysis were summarized using OBRA matrices that highlight spectral variations in the strength of the relationship between X and d for each type of relation, along with calibration scatter plots that illustrate the curve fit associated with the optimal band ratio. An example based on field spectra acquired during 10 transects across one of our Sacramento River cross sections is shown in Figure 6; analogous figures for the image data sets are included as supporting information (Figures S1–S3).

We emphasize field spectra herein because these data represent direct measurements of reflectance immediately above the water surface and thus are not contaminated by atmospheric effects, mixed pixels, or georeferencing issues that can affect image data. The relationship between X and d therefore is least ambiguous for field spectra and performing GenOBRA of this data set allowed us to highlight differences among various functional forms in the absence of the confounding influences associated with image data. In addition, because the data were essentially continuous, GenOBRA of field spectra maximized our ability to identify specific wavelengths highly sensitive to variations in depth. Insights gleaned from field spectra thus could help to direct subsequent analyses of image data sets.

For our field spectra from the upper Sacramento, all five forms of the equation used to calibrate X to d resulted in very strong relationships, with OBRA regression R^2 values greater than 0.91 in all cases and as high as 0.96 for the exponential model (Figure 6h). The plots in Figures 6f–6j indicate a moderate degree of curvature in the X versus d relation that was not captured by the linear model but was represented well by other model types, particularly the exponential. The lowess model also provided a localized fit that attempted to account for the greater variability in X that occurred at the greatest depths. The OBRA matrices in the top row of Figure 6 also were very similar to one another. Regardless of the functional form used, the optimal band pair consisted of two green wavelengths ranging from 571 to 596 nm, with the shorter of the two serving as the numerator. The broad regions of warm red tones across numerator (λ_1) wavelengths from 425 to 700 nm and denominator (λ_2) wavelengths from 500 to 725 nm indicated high OBRA R^2 values and implied that X versus d relations would remain strong even for the wider bands of multispectral and hyperspectral imaging systems. Moreover, the OBRA matrices in Figures 6a–6e indicated that many other wavelength combinations would yield X versus d relations nearly as strong as the optimal band ratio.

Similar analyses for each of the image data sets evaluated in this study confirmed the effectiveness of the GenOBRA framework for depth retrieval (Figures S1–S3). As for the field spectra, differences in the OBRA calibration R^2 among the five model types were slight, with the linear and power X versus d equations generally producing the weakest relationships and the local fitting of the lowess approach providing the highest R^2 values. Again, OBRA matrices indicated that broad ranges of wavelengths were conducive to accurate depth retrieval, not just one specific highly optimal band pair. For all three sensors, band selection

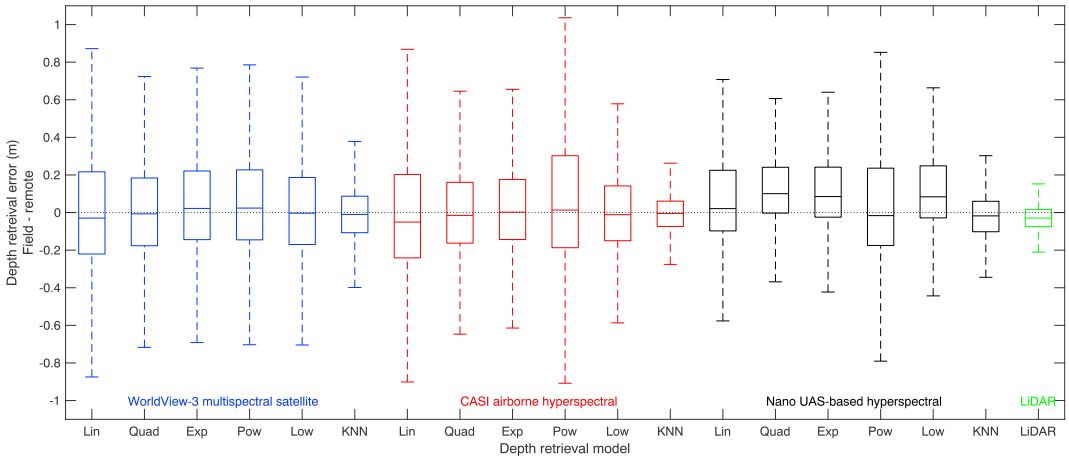

Figure 7. Box plots summarizing distributions of depth retrieval errors for six different algorithms for each of three types of passive optical image data and for a bathymetric LiDAR system. The center line of each box indicates the median and the lower and upper limits of the box correspond to the first and third quartiles. The whiskers extend above or below these quartiles by 1.5 times the interquartile range and encompass all of the data points not considered outliers. Abbreviations for the different model types are as follows: Lin = linear Optimal Band Ratio Analysis (OBRA); Quad = quadratic OBRA; Exp = exponential OBRA; Pow = power OBRA; Low = lowess OBRA; KNN = *K* nearest neighbors regression.

was not sensitive to the functional form employed, with the same (WV3) or nearly the same (CASI and Nano) wavelengths identified for all five GenOBRA variants.

3.4. Bathymetric Mapping Performance of Various Sensors and Algorithms

3.4.1. Accuracy Assessment

A number of different types of remotely sensed data are now available for mapping river bathymetry, as well as a growing number of depth retrieval algorithms. In this study, we tested the performance of six different spectrally based techniques for each of three kinds of passive optical image data (multispectral satellite and airborne and UAS-based hyperspectral) along with a water-penetrating bathymetric LiDAR system. This analysis involved comparing remotely sensed depth estimates to field-based measurements, calculating summary statistics for depth retrieval errors, and performing OP regressions. Our results are summarized in Tables 2 and S1 and depicted graphically in Figure 7.

The mean and median of the depth retrieval error ε provide a metric of accuracy and were similar and near zero for the various algorithms applied to the WV3 satellite image and CASI airborne hyperspectral image, indicating that these combinations of sensor and technique yielded unbiased depth estimates on average. For the Nano UAS-based hyperspectral image, however, mean (median) values of ε were positive and up to 8% (5%) even for an exponential OBRA relation, implying that depths tended to be underestimated from the Nano image relative to colocated field measurements. Conversely, the bathymetric LiDAR had a negative bias of 2%, suggesting that this sensor tended to slightly overpredict depth where bathymetric bottom returns were detected. Comparing WSEs derived from NIR LiDAR to 149 RTK GPS points surveyed in the field along the water's edge indicated that the LiDAR-based WSE tended to be higher than that measured in the field, with mean and median errors of −0.1 m and an error standard deviation of 0.06 m. Overestimating the WSE from the remotely sensed data might have contributed to overpredictions of depth from the bathymetric LiDAR.

We used the standard deviation of ε as a basic metric of depth retrieval precision, as well as the interquartile range that defined the lower and upper limits of the box plots in Figure 7. Error standard deviations varied slightly among the different GenOBRA variants for each sensor but overall the CASI and Nano hyperspectral images yielded more precise depth estimates (14–15% of the reach-averaged mean depth) than the WV3 satellite image (18%). For all three sensors, the new KNN algorithm resulted in smaller error standard deviations than any of the OBRA models, most notably for the WV3 image (13%). The LiDAR provided the most precise depth information, with an error standard deviation of 5%, but the maximum depth detected by the LiDAR was 2.17 m, and as a result, bathymetric coverage was only achieved for 47% of the upper Sacramento River project area.

Water Resources Research

10.1029/2018WR023586

Table 2
Depth Retrieval Error Summary Statistics

Sensor	WV3 multispectral satellite						CASI airborne hyperspectral						Nano UAS-based hyperspectral						Bathymetric
Model	Lin	Quad	Exp	Pow	Low	KNN	Lin	Quad	Exp	Pow	Low	KNN	Lin	Quad	Exp	Pow	Low	KNN	LiDAR
Validation *n*	20618	20618	20618	20618	20618	20620	21503	21503	21503	21503	21503	21503	18069	18069	18069	18069	18069	18074	13358
Mean depth (m)	1.84	1.84	1.84	1.84	1.84	1.84	1.80	1.80	1.80	1.80	1.80	1.80	1.77	1.77	1.77	1.77	1.77	1.77	1.80
Mean error (%)	1	1	3	3	1	0	0	1	2	4	0	0	6	8	8	4	7	−1	−2
Std. dev. (%)	20	18	18	18	18	13	18	14	14	21	13	10	17	14	15	20	15	12	5
Min. error (%)	−66	−85	−66	−64	−69	−62	−50	−60	−63	−74	−78	−81	−48	−45	−78	−56	−87	−96	−42
First quartile (%)	−12	−10	−8	−8	−9	−6	−13	−9	−8	−10	−8	−4	−6	0	−1	−10	−2	−6	−4
Median error (%)	−2	0	1	1	0	−1	−3	−1	0	1	−1	0	1	6	5	−1	5	−1	−2
Third quartile (%)	12	10	12	12	10	5	11	9	10	17	8	3	13	14	14	13	14	3	1
Max. error (%)	108	93	96	97	92	90	112	96	91	99	93	85	95	94	97	110	94	78	77
OP R^2	0.67	0.73	0.73	0.73	0.74	0.87	0.75	0.85	0.85	0.74	0.87	0.92	0.79	0.88	0.86	0.73	0.86	0.90	0.95
OP slope	1.01	1.01	1.02	1.05	1.02	1.01	1.01	0.99	1.03	1.42	0.99	0.99	1.12	1.20	1.20	1.29	1.20	1.02	0.96
OP intercept	0.00	0.01	0.02	−0.03	−0.02	0.00	−0.02	0.03	−0.03	−0.65	0.03	0.01	−0.11	−0.18	−0.19	−0.43	−0.21	−0.05	0.02

Note. CASI = Compact Airborne Spectrographic Imager; OP = observed versus predicted; KNN = *K* nearest neighbors regression; WV3 = WorldView-3.

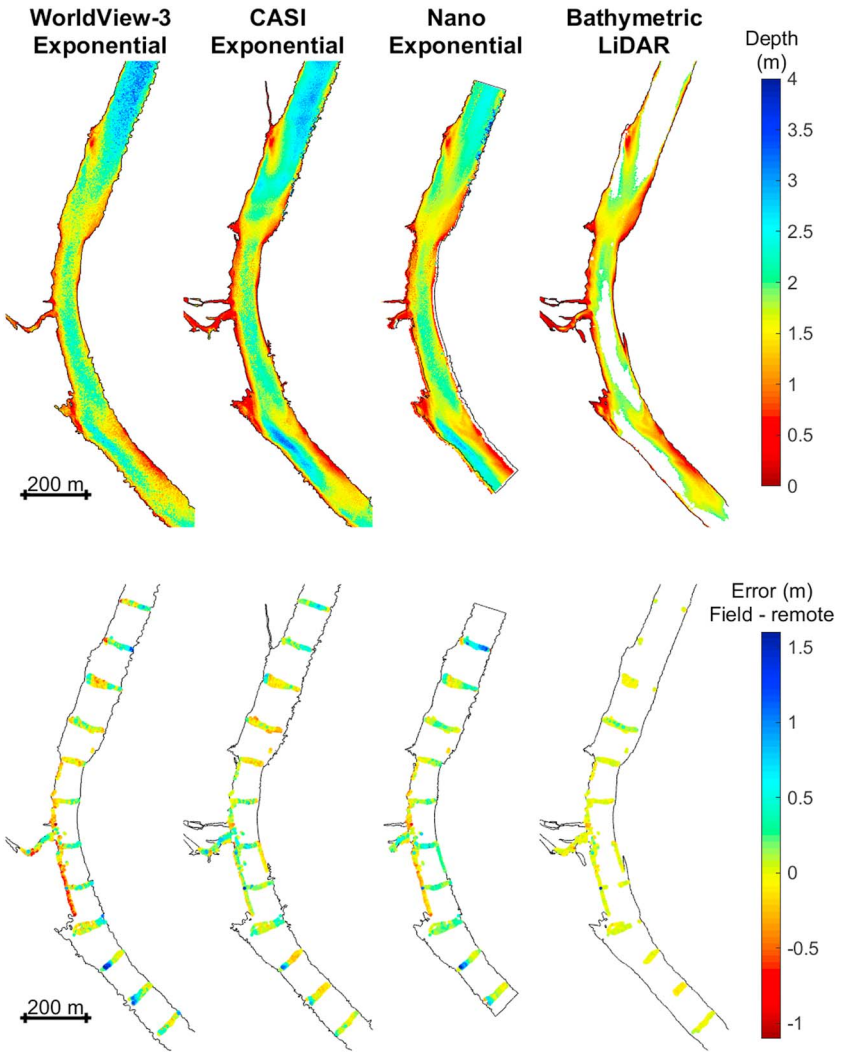

Figure 8. Remotely sensed bathymetric maps (top row) and corresponding depth retrieval error maps (bottom row) produced using an exponential Optimal Band Ratio Analysis model for the WorldView-3 multispectral satellite image and the airborne CASI and unmanned aircraft system-based hyperspectral images and for the LiDAR system. Similar figures for other depth retrieval algorithms are provided as supporting information (Figures S4–S8). CASI = Compact Airborne Spectrographic Imager.

To summarize our validation of depths inferred with various sensors and algorithms, we regressed observed depths measured in the field against predicted depths derived from remotely sensed data. The OP regression R^2 value provided a convenient metric of agreement between measured and inferred depths and ranged from 0.67 for linear OBRA of the WV3 image to 0.95 for the LiDAR. Other OBRA variants lead to higher R^2 values for the satellite data, up to 0.74 for a lowess model, but both of the hyperspectral images yielded more accurate depth estimates by this measure. For the airborne CASI data, the quadratic, exponential, and lowess versions of OBRA lead to OP regression R^2 values from 0.85 to 0.87, whereas the linear and power OBRA models were notably poorer (0.74–0.75). Results for the UAS-based Nano image were similar but slightly better, with OP R^2 values as high as 0.88 for a quadratic X versus d relation. Again, the KNN method improved depth retrieval performance in terms of OP regression, with the greatest increase in R^2 for the WV3 data set (0.87). In this study, the most reliable bathymetric information was derived from the LiDAR system, although our validation exercise only considered the subset of the channel for which bottom returns were detected; voids in the LiDAR were not included in the analysis. Inspection of the OP regression coefficients in Table 2 indicated that slopes were near 1 and intercepts near 0 for the WV3 and CASI images, implying unbiased depth retrieval for these sensors. For the UAS-based Nano image, however, slopes greater than 1 and negative intercepts implied underpredictions of depth, consistent with the error summary statistics

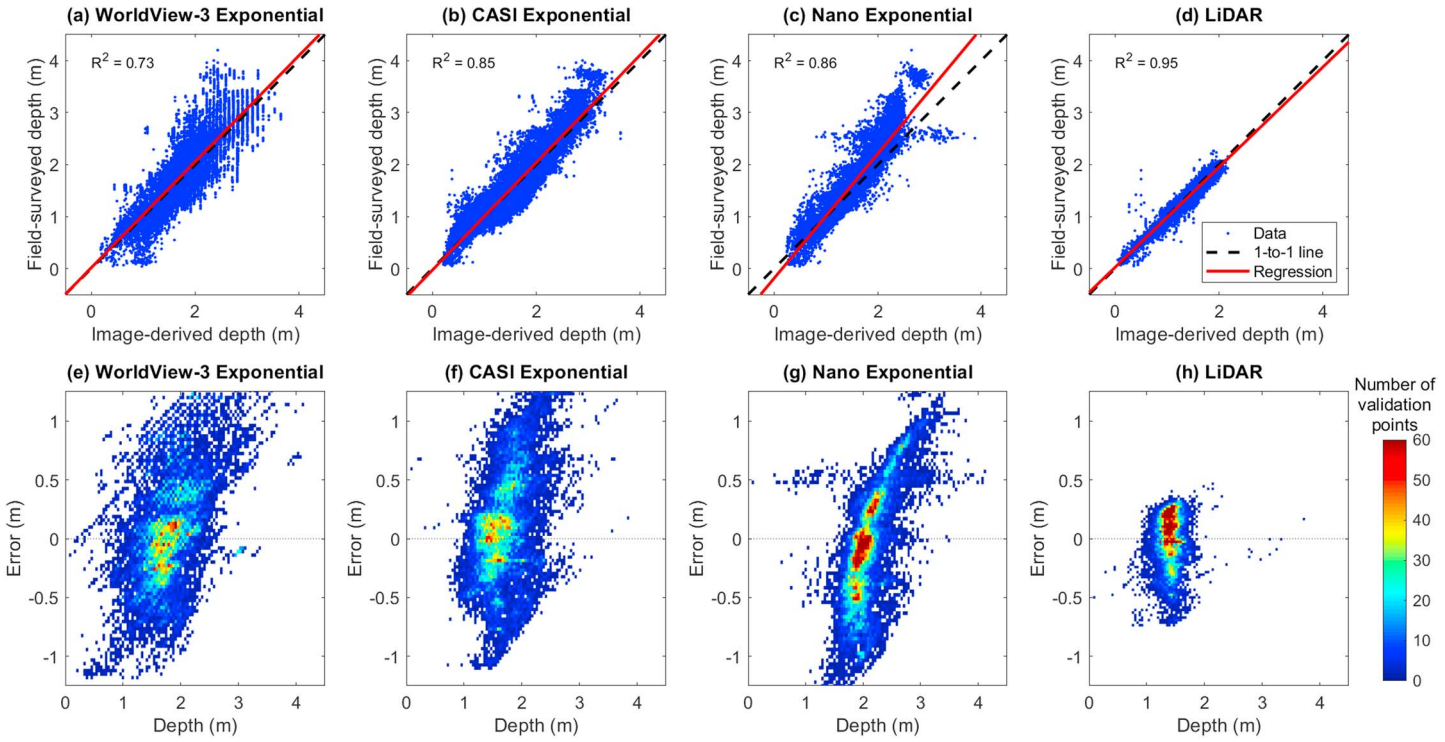

Figure 9. (a–d) Observed (field measured) versus predicted (remotely sensed) scatter plots and (e–h) plots of depth retrieval error (field - remote) as a function of measured depth for an exponential Optimal Band Ratio Analysis model applied to the three passive optical imaging systems and for the bathymetric LiDAR. Similar figures for other depth retrieval algorithms are provided as supporting information (Figures S9–S13). CASI = Compact Airborne Spectrographic Imager.

described above. Conversely, for the LiDAR an OP slope less than 1 and a small positive intercept implied a slight tendency to overpredict depths.

3.4.2. Spatial Patterns of Depth Retrieval Error

In addition to quantifying overall bathymetric mapping performance on a large gravel-bed river, a related research objective was to better understand the limitations of various sensors and algorithms by examining how accuracy varied spatially within the context of channel morphology. To support this analysis, we produced bathymetric maps and depth retrieval error maps like those shown in Figure 8 for exponential OBRA models developed for the WV3 multispectral satellite image and the CASI airborne and Nano UAS-based hyperspectral images, as well as the LiDAR. Analogous figures for other OBRA variants and the KNN algorithm are provided as supporting information (Figures S4–S8). Spatial patterns were similar across depth retrieval techniques and the following interpretations based on the exponential OBRA results depicted in Figure 8 also pertain to the other, supporting figures.

The depth maps in the top row of Figure 8 all captured the shallow areas on the right bank near the upper end of the reach where a small side channel enters the Sacramento from the floodplain, at the mouth of Cottonwood Creek at the apex of the bend, and over the point bar on the left side of the channel where the river curves to the left. The greatest depths in our study area were observed at the top of the reach and near the right (outer) bank downstream of the bend apex. These pools were best represented in the bathymetric map produced from the CASI image but were conspicuously absent from the LiDAR-based bathymetry due to the lack of bottom returns not only from these areas but anywhere the channel was deeper than about 2 m. The WV3-derived depth map was similar to that from the CASI and highlighted the pool at the upper end of the study reach but was noisier and more pixelated due to the coarser 1.36-m spatial resolution of the satellite image data (Table 1). The UAS-based Nano imaging system covered a slightly smaller spatial extent but provided the highest spatial resolution and yielded a bathymetric map that appeared relatively smooth, at least at the scale of the entire study area. Depths tended to be underpredicted from the Nano image, particularly in the pool at the top of the reach.

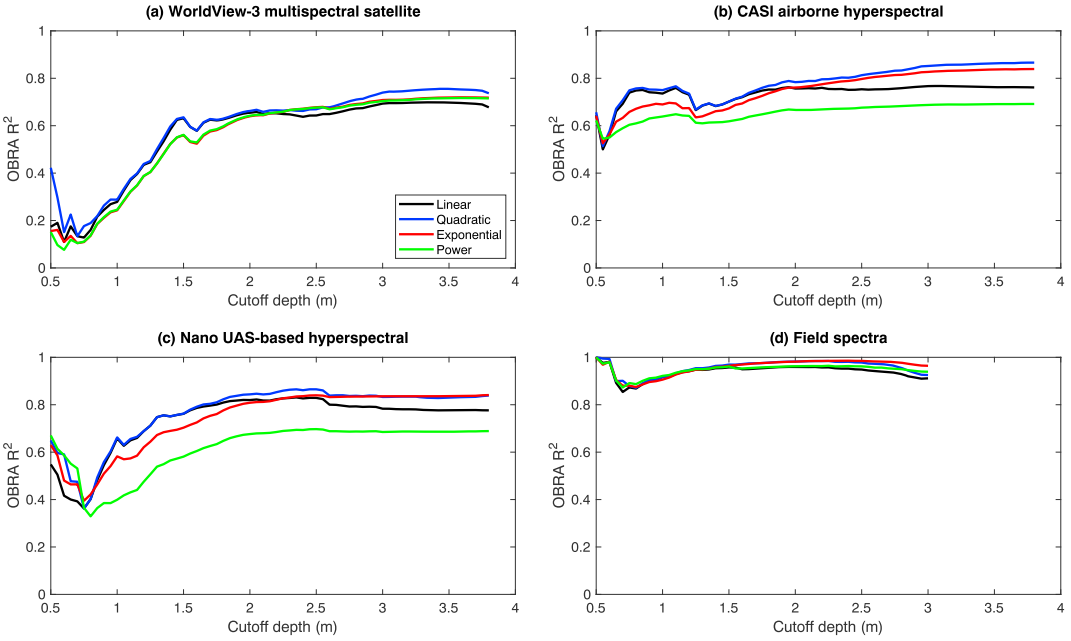

Figure 10. Generalized OBRA of Progressively Truncated Input Depths (OPTID) for three passive optical imaging systems and field spectra. The OBRA calibration R^2 is plotted against the OBRA of Progressively Truncated Input Depths cutoff depth to quantify depth retrieval performance across a range of depths. The lines in each panel represent different OBRA models. CASI = Compact Airborne Spectrographic Imager; OBRA = Optimal Band Ratio Analysis; UAS = unmanned aircraft system.

The spatial patterns in these remotely sensed bathymetries propagated to the depth retrieval error maps in the bottom row of Figure 8. For example, the warm, reddish tones adjacent to and downstream of the mouth of Cottonwood Creek in the error map for the WV3 image indicate that depths were overestimated in this area. Conversely, the dark blue symbols further downstream near the right bank represent underpredictions of depth in this pool. For the CASI error map, in contrast, overpredictions near the confluence were absent or not as evident and underpredictions in pools were smaller in terms of both magnitude and spatial extent. The overall tendency to underpredict depths from the Nano image was expressed by the green colors comprising most of the error map for this sensor. The depth retrieval error map for the LiDAR was dominated by neutral yellow tones representing very small errors in areas where depth estimates were possible but also featured large gaps where no bottom returns were detected.

3.4.3. Depth Retrieval Performance Across a Range of Depths

To evaluate the potential of various sensors and algorithms to provide reliable bathymetric information across a range of depths, we examined plots of observed vs. predicted depths, plotted depth retrieval errors as a function of measured depth, and performed OPTID. For the OP regressions and plots of error versus depth, we again used output from exponential OBRA models applied to the three passive optical images as an example (Figure 9); analogous figures for the other algorithms are provided as supporting information (Figures S9–S13).

As summarized by the OP regression R^2 values listed in Table 2 and described above, bathymetric information inferred from the WV3 image was the least reliable of the four sensors, with more scatter about the regression line in Figure 9a, particularly for greater depths. Conversely, the bathymetric LiDAR provided highly accurate, precise depth estimates, but only for areas shallower than 2 m. The two hyperspectral imaging systems were intermediate in terms of OP R^2, but departures from the best fit line were more random and evenly distributed for the CASI than for the Nano.

Plotting depth retrieval errors against observed depth further clarified how bathymetric accuracy and precision varied with depth. The plots in Figures 9e–9h can be interpreted as two-dimensional histograms, with the colors representing the density of observations; warm red tones indicate a higher concentration of data points for a particular combination of d and ε. The distribution of errors was broadest for the WV3 image and narrowest for the LiDAR, consistent with the accuracy assessment in section 3.4.1. Visualizing

the data in this manner, however, revealed that the error distribution varied with depth for the three passive optical imaging systems and was not symmetric about 0, as would occur for an ideal bathymetric mapping instrument. In all cases, depths tended to be overpredicted (negative errors) for shallower depths and underpredicted (positive errors) for relatively large observed depths. This pattern was expressed as a positive trend in the ϵ versus d scatter plots in Figures 9e–9g. The negative bias toward underprediction of depths for the Nano image was highlighted by the dark red area below the dashed horizontal line for zero error in Figure 9g. The LiDAR system provided the most symmetric, least skewed error distribution but was based almost entirely on shallow depths less than 2 m due to the extensive voids in this data set.

The new OPTID procedure introduced by Legleiter et al. (2018) also provided an explicit means of quantifying depth retrieval performance across a range of depths. Figure 10 shows that OBRA R^2 initially decreased with cutoff depth when the calibration data set was restricted to include only a very small range of depths up to about 0.75 m. With further increases in cutoff depth, however, OBRA R^2 increased as a broader range of depths were included in the calibration data sets. This positive trend continued over the entire range of cutoff depths for the WV3 and CASI images but for the Nano image OBRA R^2 dropped slightly at 2.55 m and then remained steady at a plateau of 0.69–0.84, depending on OBRA model type. For the field spectra, OBRA R^2 reached a maximum of 0.98 for a cutoff depth of 2.3 m before decreasing slightly for greater depths. In all cases, the plots of OBRA calibration R^2 did not feature any obvious, pronounced inflection points beyond which the OBRA R^2 decreased with cutoff depth. Moreover, the similarity among the lines representing different OBRA models in each panel of Figure 10 suggests that none of the OBRA variants provided markedly superior performance for certain ranges of depths, although the linear and power models were noticeably worse for the two hyperspectral image data sets.

In contrast to the passive optical imaging systems, the Riegl VQ-880-G LiDAR we evaluated failed to provide depth information across the full range of depths present in our study area along the Sacramento River. The depth distributions measured in the field and inferred from the LiDAR and airborne hyperspectral imaging systems are compared in Figure 11. Whereas the histograms for the in situ and CASI-derived depths were similar to one another, with a small underrepresentation of depths greater than about 3 m in the image-based distribution, the histogram of LiDAR depths was quite distinct from that of the field data. For over 50% of the locations with field-based depth measurements, a LiDAR-derived depth estimate could not be made due to a lack of bottom returns in areas deeper than about 2 m. The distribution of LiDAR depths in Figure 11a thus was strongly skewed toward shallower portions of the channel and essentially truncated at 2 m, implying that a large fraction of the river was not captured by this remote sensing approach. These results were expressed spatially as large voids in the bathymetric LiDAR map in Figure 8.

4. Discussion

4.1. Constraints on Remote Sensing of River Bathymetry

Reliable, spatially distributed information on water depth is critical for numerous applications in river research and management. For example, on the upper Sacramento accurate bathymetry is an essential input to decision support tools intended to help guide operation of Shasta and Keswick Dams so as to provide flow conditions favorable for federally listed salmonid species (e.g., Danner et al., 2012). More generally, depth maps facilitate in-stream habitat assessment for various organisms and monitoring of natural resources popular for recreation. In a geomorphic context, bathymetric data can be used to parameterize numerical models of flow and sediment transport, identify zones of erosion and deposition, and create morphologic sediment budgets. Given the difficulty and expense of surveying even short reaches via conventional field methods, all of these applications could benefit from improved methods for remote sensing of river bathymetry. In this study, we evaluated several new spectrally based techniques, along with various sensors and platforms. While the results we obtained from the large, gravel-bed upper Sacramento River were encouraging in some respects, certain constraints on depth retrieval must be acknowledged as well.

One critical limitation of fluvial remote sensing is that a given imaging system deployed above a specific river can only detect depths up to some finite maximum, d_{max}. For a particular combination of sensor and stream, d_{max} depends on both various river attributes and technical characteristics of the sensor itself, primarily the instrument's radiometric resolution (Legleiter & Roberts, 2009; Philpot, 1989). The IOPs of the water column exert a primary control on d_{max}, and in this study we measured beam absorption and attenuation coefficients across a range of wavelengths, as well as the backscattering coefficient at 700 nm. We compared our observations from the upper Sacramento to similar data sets from other rivers (Figures 3 and 4) as part

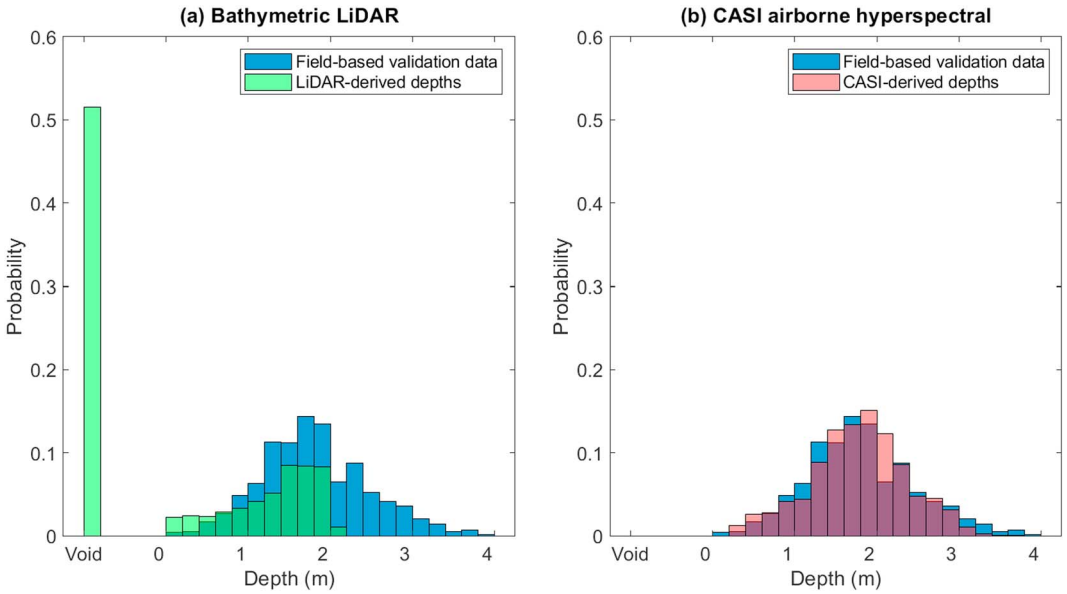

Figure 11. Histograms comparing the distribution of depths measured in the field and used for validation to the distributions of depths inferred from (a) bathymetric LiDAR and (b) airborne hyperspectral image data. Data ranges for which the distributions for the field-based validation data and remotely sensed depths overlap are represented by the superimposition of the two colors, by darker green in (a) and purple in (b). CASI = Compact Airborne Spectrographic Imager.

of an ongoing effort to quantify various factors that influence d_{max} for both passive optical and bathymetric LiDAR sensors.

In this case, the intermediate values of $a(\lambda)$ and $c(\lambda)$ for the Sacramento imply that reliable depth estimates could be inferred over a broader range of depths on the Sacramento than on more strongly attenuating rivers such as the Niobrara but also suggest that the maximum depth detectable by a given sensor would be shallower on the Sacramento than on a clear-flowing river like the Snake. We also noted that organic constituents influenced the spectral shape of $a(\lambda)$ and $c(\lambda)$, with streams carrying greater concentrations of chlorophyll and CDOM having steeper spectral slopes at blue wavelengths. This effect was most evident for the Colorado River, which had notably higher negative values of $\frac{da(\lambda)}{d\lambda}$ and $\frac{dc(\lambda)}{d\lambda}$ (Figure 3a) along with greater concentrations of chlorophyll and CDOM than all but the two least clear sites in our compilation (Muddy and Niobrara).

Suspended sediment also affects IOP's and the Sacramento again had intermediate values in comparison to the other rivers. The highly dynamic, sand-bed Niobrara River had much greater concentrations of coarser-grained material (Figures 4e and 4f) that lead to more scattering (Figure 4b), stronger attenuation (Figure 3b), and reduced water clarity (Figure 4a). The Deschutes River provides a more interesting comparison with the Sacramento. Although the water in the Deschutes appeared much darker in color than the relatively bright blue-green Sacramento, the suspended sediment concentration and D_{50} grain size were higher on the Deschutes than on the Sacramento. Figure 3a also indicates higher values of $a(\lambda)$ for the Sacramento than for the Deschutes across all wavelengths, with a similar spectral shape. For the total attenuation, however, the Sacramento had higher values of $c(\lambda)$ than the Deschutes at the shortest wavelengths on Figure 3b but attenuation was weaker on the Sacramento than on the Deschutes across the green, red, and NIR. This pattern could account for the bluish-green color of Sacramento water, driven primarily by greater scattering (Figure 4b) on the Sacramento despite its lower suspended sediment concentration and particle size. These results suggest that the composition, shape, and vertical distribution of suspended sediment within the water column also might influence a river's optical characteristics and thus d_{max}.

For passive optical image data, the iterative OPTID algorithm introduced by Legleiter et al. (2018) could provide a means of identifying the range of depths for which image-derived estimates are reliable. In this study, we generalized OPTID to include linear, quadratic, exponential, and power relations between X and d and observed similar trends on plots of the OBRA calibration R^2 versus cutoff depth for all model types

(Figure 10). For the shallowest cutoff depths, most of the available field data were excluded and a limited range of depths was used for calibration. In this case, the radiance signal related to depth was relatively weak and overwhelmed by variations in reflectance associated with differences in bottom composition, sun glint, and other types of environmental and instrumental noise. For greater cutoff depths, OBRA R^2 increased as a broader range of depths was included in the calibration data set, strengthening the depth-related signal. These results imply that a sufficient range of depths must be sampled in the field and incorporated into the calibration process to develop robust X versus d relations.

Beyond a certain cutoff depth, however, including deeper field observations could lead to decreases in OBRA R^2 as measurements greater than the sensor's d_{max} weaken the relationship between X and d. Legleiter et al. (2018) hypothesized that this scenario would be expressed as an inflection point on a plot of OBRA R^2 versus OPTID cutoff depth that could be interpreted as an estimate of the sensor's d_{max}. Importantly, this approach would allow d_{max} to be inferred directly from an image, rather than calculated on the basis of optical field measurements requiring specialized instrumentation. Legleiter et al. (2018) observed a clear inflection point in their study of the Deschutes River and reported that the maximum depth detectable by the CASI imaging system on the Deschutes was approximately 3.6 m. In this study, the absence of clear inflection points for any of the three sensors or four OBRA variants we considered suggests that all of these sensors and algorithms were capable of detecting depths up to at least 3.8 m on the upper Sacramento.

Conversely, the Riegl VQ-880-G bathymetric LiDAR system failed to provide depth information for large portions of the channel due to a lack of bottom returns from areas deeper than about 2 m. As a result, over half of our study reach was represented as voids in the LiDAR data set (Figure 11). The causes of these extensive gaps were not immediately obvious but could include excessive water turbidity, low bottom reflectance, insufficient laser power, and/or difficulties in distinguishing among returns from the water surface, water column, and streambed while processing the raw LiDAR data. Further investigation into the limitations of bathymetric LiDAR in this and other river environments is an important topic for additional research. For example, in this study we evaluated the raster data product provided by the flight contractor but careful analysis of the original point cloud and/or raw waveforms might increase the number of bottom returns. The dynamic range attainable by various LiDAR systems is often specified in terms of secchi disk depth (not measured on the Sacramento during this study), but these guidelines should be rigorously tested across a range of river environments and could be based on more objective, consistent parameters such as the IOPs of the water column.

Given these constraints on remote sensing of river bathymetry, a hybrid field and airborne approach might be required. While remote sensing can provide more continuous, more extensive spatial coverage and higher spatial resolution than traditional field surveys, remote sensing methods are limited to a certain range of depths. Rather than being viewed as a complete solution for bathymetric mapping, remote sensing techniques could be complemented by ground-based data collection. For example, image- or LiDAR-derived depth estimates for shallow areas that comprise the majority of the channel could be combined with boat-based measurements that target deep pools and any other gaps in the remote sensing coverage. The field surveys might consist of (1) a longitudinal profile down the thalweg, which would capture deep areas of the channel where remotely sensed bathymetry would be least reliable or not available at all and (2) carefully selected cross sections that could be used to characterize transverse variations in depth, provide shallow observations for calibrating remotely sensed depth estimates, and quantify depth measurement error by making multiple passes.

4.2. Selecting a Platform, Sensor, and Algorithm for Depth Retrieval

While the limitations described above must be acknowledged, these constraints do not imply that remote sensing cannot play an important role in characterizing river systems. To the contrary, a range of sensors and algorithms can provide valuable bathymetric information under appropriate circumstances. Consequently, a key challenge in fluvial remote sensing is identifying the most appropriate type of data to collect given project goals, river characteristics, and financial constraints. Making informed, efficient use of these tools requires knowledge of the various instruments and techniques available and in this study we attempted to inform these choices by acquiring remotely sensed data from various platforms and sensors and evaluating different depth retrieval algorithms. A clear understanding of study objectives is also critical, as the goals of the project, the size of the river, and the extent of the area of interest will dictate which approach is most suitable.

For example, multispectral satellite images, with their greater spatial extent and moderately high resolution, might be the preferred data type for investigating long segments of middle- to large-size rivers or for examining fluvial processes at a catchment scale (e.g., Hugue et al., 2016). Conversely, if only short reaches and/or smaller channels are of interest and fine-scale information is important, a UAS-based multispectral or hyperspectral sensor might be a better choice due to the high resolution (pixel sizes of a few cm to tens of centimeters) that can be achieved and the ability to tailor flight plans and data collection parameters on a case-by-case basis. Imaging systems deployed from manned, fixed-wing aircraft might be the most versatile, providing spatial resolution intermediate between satellite data and UAS and enabling targeted, task-specific data collection along river corridors at an extent that would be comparable to that captured in a typical satellite image and would be impractical to cover via UAS.

Another important consideration during sensor selection could be operational flexibility. For example, deployment from a UAS would enable opportunistic data collection under favorable conditions, avoiding flashfloods that might reduce water clarity, smoke from fires that might impede visibility, or other factors that might compromise image acquisition. UAS also have greater rapid response potential for capturing transient events of interest, such as salmon spawning runs, blooms of benthic algae, or geomorphic change detection after a flood (e.g., Tamminga et al., 2015). Whereas UAS can be operated independently by small research groups or agencies, provided appropriate certifications and permissions are in place, airborne data collection typically entails working with a flight contractor and thus involves a longer planning horizon and greater coordination. Similarly, although satellites can be tasked for specific areas of interest and an acquisition window requested, the end user has no control over the exact timing of data collection. Clouds or haze also could render a satellite image useless. Planning a fluvial remote sensing study will involve trade-offs related to (1) area of coverage; (2) sensor characteristics, such as spatial, spectral, and radiometric resolution; (3) operational parameters, including flying height, speed, and survey duration for UAS or aircraft; and (4) cost, of course. Potential users should anticipate making a careful, deliberate decision as to which remote sensing approach is most likely to meet a study's objectives.

An encouraging result of our investigation on the upper Sacramento River was the strong depth retrieval performance of the WV3 multispectral satellite. This orbital platform features off-nadir pointing capabilities that allow for short revisit times and enable the sensor to be tasked for specific locations. Moreover, because WV3 data are available to U.S. government agencies at no cost through a special licensing program called NextView and also are relatively affordable for nongovernmental organizations, this approach could become a powerful tool for assessment and monitoring of in-stream habitat and other applications in river management. Our analysis of WV3 images with varying levels of preprocessing indicated that reliable bathymetric information could be derived from a standard, basic WV3 data product. The OBRA results summarized in Figure 5 imply that even for images comprised of raw, uncalibrated digital numbers, taking the ratio of two spectral bands accounted for sensor characteristics and atmospheric influences and successfully isolated the effect of depth on pixel values. Moreover, accurate depth estimates can be produced from minimally processed satellite image data, without requiring more advanced, specialized remote sensing software and expertise. A caveat to the potential utility of WV3 data for this purpose is that the sensor's relatively low radiometric resolution, along with atmospheric effects, could reduce the signal-to-noise ratio of satellite images and cause the radiance signal to saturate in deeper water, with further increases in d no longer leading to corresponding changes in the image-derived quantity X. In addition, the basic image data product required some additional georeferencing to ensure alignment with our field measurements, but we have developed an orthorectification workflow that can be applied to other projects.

In addition to evaluating data acquired by four different types of remote sensing instrument, this study also quantified the performance of several distinct depth retrieval algorithms. More specifically, we emphasized OBRA and expanded upon the OBRA framework by considering new forms of the relation between X and d. As originally formulated, OBRA performed simple linear regressions of X versus d, but coastal researchers (e.g., Dierssen et al., 2003) and subsequent work in rivers (Legleiter & Overstreet, 2012) showed that incorporating an X^2 term into the regression could improve depth retrieval from deeper channels. We observed artifacts in previous applications of these two models, however, primarily negative depth estimates along shallow channel margins for linear OBRA and overestimates of depth near the banks when using a quadratic formulation.

In this study, we added exponential and power X versus d relations as a means of generalizing the calibration process and circumventing some of the issues associated with simpler linear and quadratic models. For example, describing the relationship between X and d with an exponential equation (4) avoided the parabolic shape of a quadratic, which can produce spurious overpredictions of depth for relatively small values of X (Legleiter et al., 2018), and replaced it with a monotonically increasing X versus d relation that yielded more realistic estimates in both shallow and deep areas. In addition, an exponential function will not yield negative depth estimates for small X values, as can occur for linear OBRA. Because the exponential formulation eliminated these artifacts and provided accuracies as good or better than any of the other GenOBRA models, our results suggest that an exponential function might be the preferred type of X versus d relation for depth retrieval.

In addition, our analysis of continuous spectra measured directly in the field indicated that the optimal wavelengths for depth retrieval were consistent across the different OBRA variants: a numerator band around 572 nm and a denominator around 592 nm (Figure 6). The ability to distinguish among these two optimal wavelengths, separated by only 20 nm and both within the green portion of the visible spectrum, represents an advantage of using hyperspectral rather multispectral image data for bathymetric mapping and could account for the superior depth retrieval performance of the CASI and Nano imaging systems. This portion of the spectrum might have been particularly sensitive to variations in depth due to the steep spectral slope that occurred around 580 nm where scattering-dominated radiative transfer at shorter wavelengths transitioned to absorption-dominated radiative transfer at longer wavelengths, as observed in simulated spectra produced using a radiative transfer model (Legleiter et al., 2009). Nevertheless, the extensive warm, red tones indicating high OBRA R^2 values not only for the field spectra in Figure 6 but also the various passive optical image data sets in Figures S1–S3 imply that a broad range of wavelengths could be used for depth retrieval. These results suggest that even if a sensor's bands do not exactly coincide with the optimal pair of wavelengths identified via field spectroscopy, accurate depth estimates could be derived from multispectral images. Similarly, the generalized OPTID analysis summarized in Figure 10 indicated that plots of OBRA R^2 versus cutoff depth were similar across OBRA models, implying that the none of the models performed noticeably better or worse than any of the others for certain ranges of depth. The choice of an appropriate X versus d relation thus could be based on a simpler evaluation of overall depth retrieval accuracy rather than the more involved, iterative OPTID algorithm.

As an alternative to OBRA, we also considered the KNN approach. Kibele and Shears (2016) first applied this nonparametric technique in the context of spectrally based depth retrieval using WorldView-2 satellite images of a coastal environment and found that KNN produced more accurate depth maps than the widely used approximate radiative transfer model of Lyzenga (1978). Because KNN is applicable to images with minimal preprocessing (i.e., no atmospheric correction), the algorithm does not require specialized remote sensing software or expertise. Similarly, KNN could be applied across a broader range of environmental conditions than more complex, physics-based methods that often involve numerous assumptions. In our study of the upper Sacramento River, KNN provided a high level of depth retrieval performance superior to any of the OBRA variants, with the most pronounced improvement observed for the WV3 data set (Figure 7 and Table 2). These results imply that this machine learning approach could facilitate depth retrieval, particularly for multispectral satellite images.

The principal drawback of KNN is that the technique is purely empirical and thus inherently site specific and scene specific, that is, only applicable to the image for which the algorithm is trained. The same is true for the lowess-based version of OBRA we examined, as depth estimates produced via lowess were essentially interpolated values generated by smoothing an X versus d scatter plot. Moreover, KNN cannot be used to extrapolate beyond the range of field-based depth measurements provided as training data. Thus, although KNN is an appealing alternative approach, the utility of this technique will depend on the need for generality, which might favor an OBRA model (except for lowess), versus the value of improved local accuracy, which might take precedence if only a relatively short reach encompassed within a single image is of interest. In addition, the KNN technique could be generalized to some degree if multiple images could be normalized to one another.

4.3. Future Research Directions

The appeal of remote sensing is the potential to provide continuous, spatially distributed information on various river attributes with a level of detail (i.e., resolution) and extent (i.e., coverage) that would be dif-

ficult, if not impossible, to achieve via traditional field methods. This capability, however, has not been demonstrated at the larger scales that are of greatest interest for river management applications such as the spawning habitat inventory of the upper Sacramento River for which the data sets we examined were acquired. Although this study reported some encouraging results regarding the depth retrieval performance of three different types of passive optical image data and, to a lesser degree, a bathymetric LiDAR, this analysis was based on field data collected from a single, short reach. As articulated by Legleiter et al. (2016), this type of localized validation is not necessarily a complete, rigorous evaluation of the utility of a particular remote sensing approach at the larger scales at which we ultimately intend to apply the technology. In other words, producing accurate bathymetric maps for our 1.6-km study reach at the Cottonwood Creek confluence does not necessarily indicate that a similar level of performance could be achieved over the entire 112 km of the upper Sacramento River for which remotely sensed data were collected. However, this reach-scale, proof-of-concept investigation of different platforms, sensors, and depth retrieval algorithms was a necessary first step toward broader applications of remote sensing.

Given the numerous challenges involved in scaling up from reach to segment to watershed scales, thoroughly testing the capabilities of various sensors and algorithms over many tens of hundreds of river kilometers emerges as a priority for future research. Ensuring consistent, reliable depth retrieval at these larger scales will require addressing a number of issues, including (1) normalizing images, at least via a basic radiometric calibration and ideally involving a full atmospheric correction; (2) establishing robust, general relations between image-derived quantities and water depth that are applicable at a watershed rather than just a reach scale, even in the presence of variable bottom types, sediment sources, water column optical properties, riparian vegetation, and shadowing; and (3) assessing the accuracy of any candidate bathymetric mapping algorithm using field measurements at multiple locations that are spatially distinct from the site or sites used to train the algorithm (Legleiter et al., 2016). Although this study introduced some new techniques and considered a broader range of sensors and platforms, our initial evaluation was limited to the single, short reach for which a detailed field-based survey was available. Future work will focus on collecting more extensive field data sets and tackling the myriad challenges involved in scaling up to realize the full potential of remote sensing to facilitate river research and management.

In pursuing this goal, we will be particularly interested in further testing our ability to map the bathymetry of long river segments from multispectral satellite image data. In the current study, even basic, uncalibrated WV3 data provided accurate depth estimates for a short reach encompassed within a single image, but characterizing habitat conditions along the full extent of the upper Sacramento in which we are ultimately interested will entail working with a mosaic comprised of multiple satellite scenes. Such a collection of images would need to be standardized to a consistent radiometry. Similarly, the generality of depth-reflectance relations derived via OBRA and/or a site-specific machine learning algorithm like KNN will need to be assessed carefully. This analysis also will raise a number of other questions regarding the field-based sampling requirements for successful, robust calibration, particularly across sites. Similarly, future studies might attempt to develop methods of predicting depth retrieval performance on the basis of optical field measurements, which would allow a more quantitative assessment of feasibility before investing in remotely sensed data.

5. Conclusion

This study evaluated the potential to map the bathymetry of a short (1.6 km) reach of the upper Sacramento River from remotely sensed data acquired from a number of different platforms by several types of instrumentation and analyzed using a range of depth retrieval algorithms. We collected field measurements of water depth to assess the performance of the various approaches and our results support the following principal conclusions:

1. The water column optical properties we measured along the Sacramento were intermediate relative to other rivers with similar data sets. Our observations of attenuation, absorption, scattering, turbidity, and constituent concentrations imply that the maximum depth detectable on the Sacramento would be greater than on sediment-laden, highly turbid streams but shallower than for relatively clear-flowing rivers.

2. Accurate depth estimates were derived from a basic WV3 multispectral satellite image data product, implying that radiometric calibration and/or atmospheric correction were not essential for depth retrieval, at least for a single scene for which field measurements were available for calibration.
3. GenOBRA of field spectra and three types of passive optical image data indicated that similar wavelength combinations were selected for depth retrieval regardless of the functional form employed. Moreover, a broad range of wavelengths provided strong relationships between the image-derived quantity X and flow depth d, implying that river bathymetry could be accurately mapped from multispectral images with a smaller number of wider bands.
4. Differences in overall depth retrieval accuracy among linear, quadratic, exponential, power, and lowess OBRA models were minor and OPTID lead to similar trends on plots of OBRA R^2 versus cutoff depth.
5. An exponential formulation emerged as the preferred version of OBRA for its ability to avoid artifacts associated with other model types, such as negative depth estimates along channel margins for linear OBRA and overpredictions of depth near the banks for quadratic OBRA, and greater generality than lowess.
6. Mean depth retrieval errors were near zero for the WV3 satellite and airborne hyperspectral sensors, but depths were underpredicted from UAS-based hyperspectral data by up to 8%. The precision of OBRA-based depth estimates was 14–15% of the mean depth for airborne and UAS-based hyperspectral data and 18% for the WV3 image.
7. The KNN machine learning algorithm improved depth retrieval performance, most notably by increasing the OP R^2 from 0.74 to 0.87 for the WV3 image, but this technique can only be applied to the image for which it is trained and does not allow for extrapolation outside the range of depths provided for calibration.
8. A bathymetric LiDAR system provided the most accurate and precise depth estimates (5% error), but only for depths up to 2 m. A lack of bottom returns from deeper areas led to large voids in the LiDAR-based depth map and further research is needed to identify factors leading to the limited range of depths detected by this sensor.
9. Bathymetric maps produced from all sensors and algorithms were spatially coherent and hydraulically reasonable, but depth retrieval error maps highlighted overestimates of depth along channel margins for the WV3 data, underpredictions of pool depth from all of the optical images, and extensive gaps in the LiDAR coverage. These patterns also were evident in plots of depth retrieval error against measured depth.
10. OPTID of field spectra and multispectral and hyperspectral images did not lead to any obvious inflection points on plots of OBRA R^2 versus cutoff depth, suggesting that the sensors we evaluated were capable of detecting depths up to 3.8 m on the Sacramento.
11. The maximum depth detectable by a particular sensor in a specific river of interest imposes an important constraint on fluvial remote sensing and a hybrid approach in combination with field-based data collection focused on the deepest areas of the channel might be a more realistic strategy for mapping river bathymetry.
12. Selecting an appropriate platform, sensor, and algorithm for depth retrieval requires a clear understanding of project objectives and involves compromises among spatial extent and resolution, operational flexibility, and cost.
13. Future research will move beyond this reach-scale, proof-of-concept study and tackle the numerous challenges involved in mapping the bathymetry of much longer river segments from remotely sensed data. This work will focus on satellite data, approaches to image normalization, and developing robust calibrations across sites.

Acknowledgments
Any use of trade, firm, or product names is for descriptive purposes only and does not imply endorsement by the U.S. Government. This investigation was supported by a grant from the Office of Naval Research Littoral Geosciences and Optics Program (Grant N000141010873). Funding for the bathymetric LiDAR and CASI hyperspectral image data was provided by the California Department of Fish and Wildlife (Grant P1610802). We would also like to acknowledge the NOAA UAS Program Office for supporting the acquisition of the Nano hyperspectral image data (Grant P1610802). Charles Kepler, Jeremy Notch, Miles Daniels, Peter Dudley, Vamsi Sridharan, Matt Pickett, Brian Taggart, and Alicia Amerson assisted with field and UAS data collection. The field measurements and image data sets used in this study are available through the USGS ScienceBase Catalog data releases listed in the references.

References

Benjankar, R. M., Tonina, D., McKean, J. A., Sohrabi, M. M., Chen, Q., & Vidergar, D. (2018). Dam operations may improve aquatic habitat and offset negative effects of climate change. *Journal of Environmental Management*, *213*, 126–134.

Bernstein, L. S., Jin, X., Gregor, B., & Adler-Golden, S. M. (2012). Quick Atmospheric Correction code: Algorithm description and recent upgrades. *Optical Engineering*, *51*(11), 12.

Bovee, K. D. (1978). The Incremental Method of assessing habitat potential for cool water species, with management implications. *American Fisheries Society Special Publication*, *11*, 340–346.

Carbonneau, P., Fonstad, M. A., Marcus, W. A., & Dugdale, S. J. (2011). Making riverscapes real. *Geomorphology*, *137*(1), 74–86.

Cleveland, W. S., & Devlin, S. J. (1988). Locally weighted regression: An approach to regression analysis by local fitting. *Journal of the American Statistical Association*, *83*(403), 596–610.

Conner, J. T., & Tonina, D. (2014). Effect of cross-section interpolated bathymetry on 2D hydrodynamic results in a large river. *Earth Surface Processes and Landforms*, *39*(4), 463–475.
Danner, E. M., Melton, F. S., Pike, A., Hashimoto, H., Michaelis, A., Rajagopalan, B., et al. (2012). River temperature forecasting: A coupled-modeling framework for management of river habitat. *IEEE Journal of Selected Topics in Applied Earth Observations and Remote Sensing*, *5*(6), 1752–1760.
Davies-Colley, R. J., & Smith, D. G. (2001). Turbidity, suspended sediment, and water clarity: A review. *JAWRA Journal of the American Water Resources Association*, *37*(5), 1085–1101.
Dierssen, H. M., Zimmerman, R. C., Leathers, R. A., Downes, T. V., & Davis, C. O. (2003). Ocean color remote sensing of seagrass and bathymetry in the Bahamas Banks by high-resolution airborne imagery. *Limnology and Oceanography*, *48*(1), 444–455.
Dietrich, J. T. (2016). Riverscape mapping with helicopter-based structure-from-motion photogrammetry. *Geomorphology*, *252*, 144–157.
Dietrich, J. T. (2017). Bathymetric structure-from-motion: Extracting shallow stream bathymetry from multi-view stereo photogrammetry. *Earth Surface Processes and Landforms*, *42*(2), 355–364.
Dilbone, E., Legleiter, C., Alexander, J., & McElroy, B. (2018). Spectrally based bathymetric mapping of a dynamic, sand-bedded channel: Niobrara River, Nebraska, USA. *River Research and Applications*, *34*(5), 430–441.
Dudley, P. N. (2018). A salmonid individual-based model as a proposed decision support tool for management of a large regulated river. *Ecosphere*, *9*(1), e02074.
Entwistle, N., Heritage, G., & Milan, D. (2018). Recent remote sensing applications for hydro and morphodynamic monitoring & modelling. *Earth Surface Processes and Landforms*, *43*(10), 2283–2291.
Fausch, K. D., Torgersen, C. E., Baxter, C. V., & Li, H. W. (2002). Landscapes to riverscapes: Bridging the gap between research and conservation of stream fishes. *BioScience*, *52*(6), 483–498.
Fonstad, M. A., Dietrich, J. T., Courville, B. C., Jensen, J. L., & Carbonneau, P. E. (2013). Topographic structure from motion: A new development in photogrammetric measurement. *Earth Surface Processes and Landforms*, *38*(4), 421–430.
Fonstad, M. A., & Marcus, W. A. (2005). Remote sensing of stream depths with hydraulically assisted bathymetry (HAB) models. *Geomorphology*, *72*(1-4), 320–339.
Glenn, J., Tonina, D., Morehead, M. D., Fiedler, F., & Benjankar, R. (2016). Effect of transect location, transect spacing and interpolation methods on river bathymetry accuracy. *Earth Surface Processes and Landforms*, *41*(9), 1185–1198.
Headwall Photonics (2018). Nano-Hyperspec, http://www.headwallphotonics.com/spectral–imaging/hyperspectral/nano–hyperspec
Hugue, F., Lapointe, M., Eaton, B. C., & Lepoutre, A. (2016). Satellite-based remote sensing of running water habitats at large riverscape scales: Tools to analyze habitat heterogeneity for river ecosystem management. *Geomorphology*, *253*, 353–369.
Innovation, Technology, Research, Excellence, and Science (ITRES) (2014). CASI-1500 Hyperspectral Imager, http://www.itres.com/products/imagers/casi1500/
Kammel, L. E., Pasternack, G. B., Massa, D. A., & Bratovich, P. M. (2016). Near-census ecohydraulics bioverification of Oncorhynchus mykiss spawning microhabitat preferences. *Journal of Ecohydraulics*, *1*(1-2), 62–78.
Kerr, J. M., & Purkis, S. (2018). An algorithm for optically-deriving water depth from multispectral imagery in coral reef landscapes in the absence of ground-truth data. *Remote Sensing of Environment*, *210*, 307–324.
Kibele, J., & Shears, N. T. (2016). Nonparametric empirical depth regression for bathymetric mapping in coastal waters. *IEEE Journal of Selected Topics in Applied Earth Observations and Remote Sensing*, *9*(11), 5130–5138.
Kinzel, P. J., Legleiter, C. J., & Nelson, J. M. (2013). Mapping river bathymetry with a small footprint green LiDAR: Applications and challenges. *Journal of the American Water Resources Association*, *49*(1), 183–204.
Kuester, M. (2016). Radiometric use of WorldView-3 imagery, DigitalGlobe Technical Note, https://dg-cms-uploads-production.s3.amazonaws.com/uploads/document/file/207/Radiometric_Use_of_WorldView-3_v2.pdf
Leclerc, M., Boudreault, A., Bechara, J. A., & Corfa, G. (1995). Two-dimensional hydrodynamic modeling: A neglected tool in the instream flow incremental methodology. *Transactions of the American Fisheries Society*, *124*(5), 645–662.
Legleiter, C. J. (2012). Remote measurement of river morphology via fusion of LiDAR topography and spectrally based bathymetry. *Earth Surface Processes and Landforms*, *37*(5), 499–518.
Legleiter, C. J. (2013). Mapping river depth from publicly available aerial images. *River Research and Applications*, *29*(6), 760–780.
Legleiter, C. J. (2015). Calibrating remotely sensed river bathymetry in the absence of field measurements: Flow Resistance Equation-Based Imaging of River Depths (FREEBIRD). *Water Resources Research*, *51*, 2865–2884. https://doi.org/10.1002/2014WR016624
Legleiter, C. J. (2016). Inferring river bathymetry via Image-to-Depth Quantile Transformation (IDQT). *Water Resources Research*, *52*, 3722–3741. https://doi.org/10.1002/2016WR018730
Legleiter, C., & Harrison, L. (2018). *Remotely sensed data and field measurements used for bathymetric mapping of the upper Sacramento River in northern California*: U.S. Geological Survey data release. https://doi.org/10.5066/F7Q52NZ1
Legleiter, C. J., Kinzel, P. J., & Overstreet, B. T. (2011). Evaluating the potential for remote bathymetric mapping of a turbid, sand-bed river: 2. Application to hyperspectral image data from the Platte River. *Water Resources Research*, *47*, W09532. https://doi.org/10.1029/2011wr010,592
Legleiter, C. J., Mobley, C. D., & Overstreet, B. T. (2017). A framework for modeling connections between hydraulics, water surface roughness, and surface reflectance in open channel flows. *Journal of Geophysical Research: Earth Surface*, *122*, 1715–1741. https://doi.org/10.1002/2017JF004323
Legleiter, C. J., & Overstreet, B. T. (2012). Mapping gravel bed river bathymetry from space. *Journal of Geophysical Research*, *117*, F04024. https://doi.org/10.1029/2012JF002539
Legleiter, C. J., Overstreet, B. T., Glennie, C. L., Pan, Z., Fernandez-Diaz, J. C., & Singhania, A. (2016). Evaluating the capabilities of the CASI hyperspectral imaging system and Aquarius bathymetric LiDAR for measuring channel morphology in two distinct river environments. *Earth Surface Processes and Landforms*, *41*(3), 344–363.
Legleiter, C., Overstreet, B., & Kinzel, P. (2018). Sampling strategies to improve passive optical remote sensing of river bathymetry. *Remote Sensing*, *10*(6), 935.
Legleiter, C. J., & Roberts, D. A. (2009). A forward image model for passive optical remote sensing of river bathymetry. *Remote Sensing of Environment*, *113*(5), 1025–1045.
Legleiter, C. J., Roberts, D. A., & Lawrence, R. L. (2009). Spectrally based remote sensing of river bathymetry. *Earth Surface Processes and Landforms*, *34*(8), 1039–1059.
Legleiter, C. J., Roberts, D. A., Marcus, W. A., & Fonstad, M. A. (2004). Passive optical remote sensing of river channel morphology and in-stream habitat: Physical basis and feasibility. *Remote Sensing of Environment*, *93*(4), 493–510.
Lyon, J. G., Lunetta, R. S., & Williams, D. C. (1992). Airborne multispectral scanner data for evaluating bottom sediment types and water depths of the St. Marys River, Michigan. *Photogrammetric Engineering and Remote Sensing*, *58*(7), 951–956.

Lyzenga, D. R. (1978). Passive remote-sensing techniques for mapping water depth and bottom features. *Applied Optics*, *17*(3), 379–383.
Mandlburger, G., Pfennigbauer, M., Wieser, M., Riegl, U., & Pfeifer, N. (2016). Evaluation of a novel UAV-borne topo-bathymetric laser profiler. *International Archives of the Photogrammetry, Remote Sensing and Spatial Information Sciences, XLI-B1*, 933–939.
Marcus, W. A., & Fonstad, M. A. (2010). Remote sensing of rivers: The emergence of a subdiscipline in the river sciences. *Earth Surface Processes and Landforms*, *35*(15), 1867–1872.
McKean, J. A., Isaak, D. J., & Wright, C. W. (2008). Geomorphic controls on salmon nesting patterns described by a new, narrow-beam terrestrial-aquatic LiDAR. *Frontiers in Ecology and the Environment*, *6*(3), 125–130.
McKean, J. A., & Tonina, D. (2013). Bed stability in unconfined gravel-bed mountain streams: With implications for salmon spawning viability in future climates. *Journal of Geophysical Research: Earth Surface*, *118*, 1–14. https://doi.org/10.1002/jgrf.20092
McKean, J. A., Tonina, D., Bohn, C., & Wright, C. W. (2014). Effects of bathymetric lidar errors on flow properties predicted with a multi-dimensional hydraulic model. *Journal of Geophysical Research: Earth Surface*, *119*, 644–664. https://doi.org/10.1002/2013JF002897
Mishra, D. R., Narumalani, S., Rundquist, D., & Lawson, M. (2005). Characterizing the vertical diffuse attenuation coefficient for downwelling irradiance in coastal waters: Implications for water penetration by high resolution satellite data. *ISPRS Journal of Photogrammetry and Remote Sensing*, *60*(1), 48–64.
Moyle, P., Lusardi, R., Samuel, P., & Katz, J. (2017). *State of the salmonids: Status of California's emblematic fishes 2017. Center for Watershed Sciences*. San Francisco, CA: University of California, Davis and California Trout. https://watershed.ucdavis.edu/files/content/news/SOS%20II_Final.pdf
Pasternack, G. B., Wang, C. L., & Merz, J. E. (2004). Application of a 2D hydrodynamic model to design of reach-scale spawning gravel replenishment on the Mokelumne River, California. *River Research and Applications*, *20*(2), 205–225.
Philpot, W. D. (1989). Bathymetric mapping with passive multispectral imagery. *Applied Optics*, *28*(8), 1569–1578.
Pike, A., Danner, E., Boughton, D., Forrest, M., Rama, N., Balaji, R., & Lindley, S. (2013). Forecasting river temperatures in real time using a stochastic dynamics approach. *Water Resources Research*, *49*, 5168–5182. https://doi.org/10.1002/wrcr.20389
Pineiro, G., Perelman, S., Guerschman, J. P., & Paruelo, J. M. (2008). How to evaluate models: Observed vs. predicted or predicted vs. observed? *Ecological Modelling*, *216*(3-4), 316–322.
ReSe (2014). ATCOR 4: Atmospheric & topographic correction for wide FOV airborne optical scanner data, http://www.rese.ch/products/atcor/atcor4/
Riegl (2018). Riegl VQ-880-G, http://www.riegl.com/nc/products/airborne-scanning/produktdetail/product/scanner/46/
Smith, M., Carrivick, J., & Quincey, D. (2016). Structure from motion photogrammetry in physical geography. *Progress in Physical Geography*, *40*(2), 247–275.
Tamminga, A. D., Eaton, B. C., & Hugenholtz, C. H. (2015). UAS-based remote sensing of fluvial change following an extreme flood event. *Earth Surface Processes and Landforms*, *40*(11), 1464–1476.
Williams, R. D., Brasington, J., Vericat, D., & Hicks, D. M. (2014). Hyperscale terrain modelling of braided rivers: Fusing mobile terrestrial laser scanning and optical bathymetric mapping. *Earth Surface Processes and Landforms*, *39*(2), 167–183.
Winterbottom, S. J., & Gilvear, D. J. (1997). Quantification of channel bed morphology in gravel-bed rivers using airborne multispectral imagery and aerial photography. *Regulated Rivers: Research & Management*, *13*(6), 489–499.
Woodget, A. S., Carbonneau, P. E., Visser, F., & Maddock, I. P. (2015). Quantifying submerged fluvial topography using hyperspatial resolution UAS imagery and structure from motion photogrammetry. *Earth Surface Processes and Landforms*, *40*(1), 47–64.